NSSI Neutron Newsletter

Number 6
December 2024

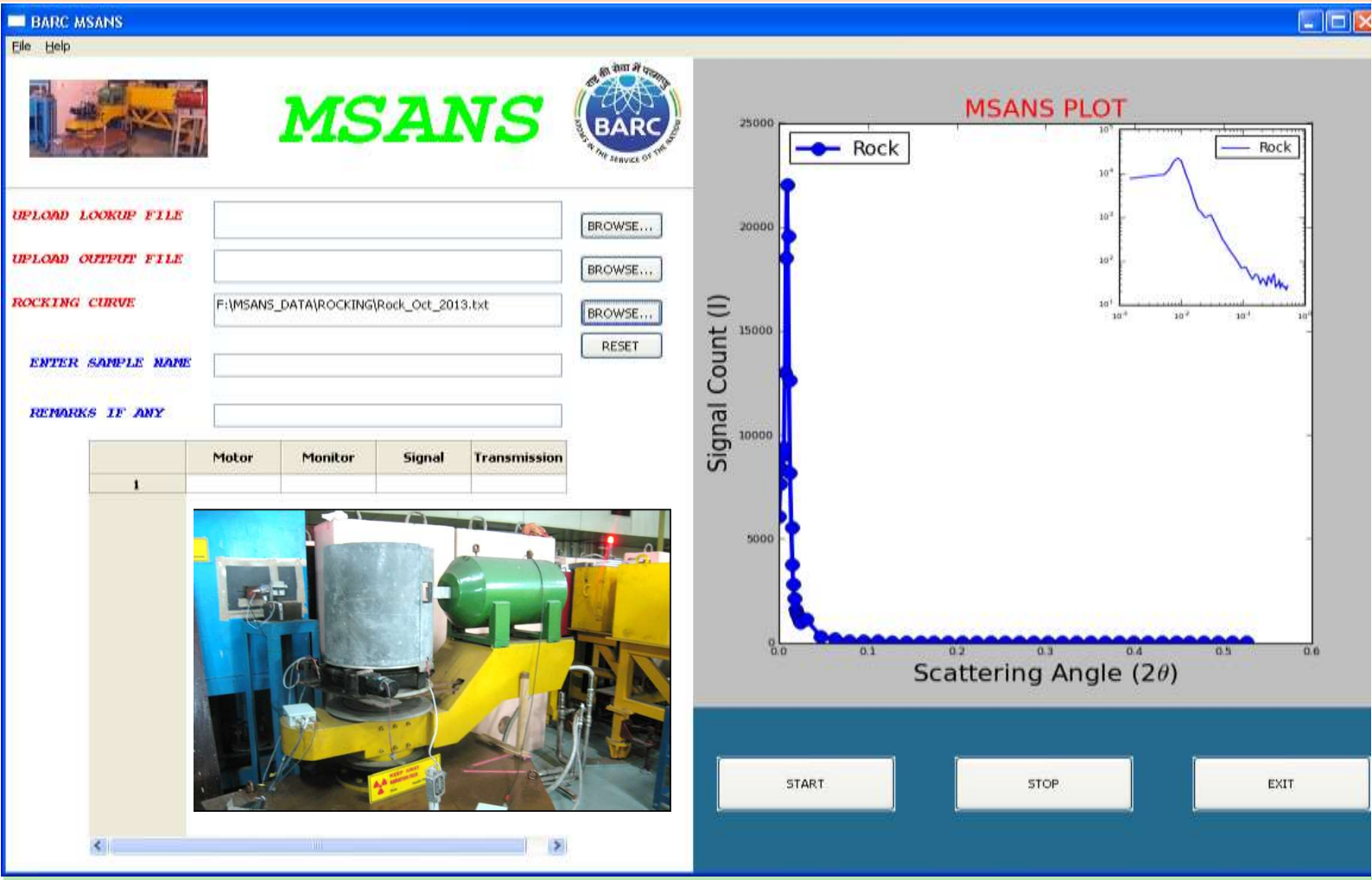

Neutron Scattering Society of India

The Neutron Scattering Society of India (NSSI) was formed in 2008 to provide a forum for neutron users to promote neutron-based research and development activities including applications in the country. The NSSI is the adhering society representing the neutron users in India to the Asia-Oceania Neutron Scattering Association (AONSA), which is an affiliation of all neutron scattering societies in the Asia-Oceania region. NSSI happens to be one of the founder members of the AONSA along with the respective neutron societies from Japan, South Korea, Australia and Taiwan. At present, NSSI has 325 registered members from various universities and institutions spread all over the country.

Cover Page

The schematic of *the python GUI based data acquisition software window for MSANS*. See the article on "*Quantifying Mesoscopic Structures in Materials: Insight from Small-Angle Neutron Scattering Experiments using Double-Crystal Based Facility at Dhruva"* by Avik Das, J. Bahadur and Debasis Sen (page 19).

Contents

- Editorial 4
- Reports as sent to AONSA from NSSI 5-6
- Highlights of Neutron Research 7-18
- A short status review on Quantifying Mesoscopic Structures in Materials: Insight from Small-Angle Neutron Scattering Experiments using Double-Crystal Based Facility at Dhruva 19-40
- Links to forthcoming Neutron Conferences and Workshops 41
- NSSI application for membership 42

Editorial

We are glad to bring out this sixths issue of the NSSI Newsletter. We would like to thank Prof. Dhananjay Pandey, the President of NSSI, for his continued guidance and support for this activity. We have also immensely benefited from the contributions from various Members of the Managing Committee of NSSI. Personally, as the Editor, I acknowledge the excellent and enthusiastic contributions from Prof. Vinod Aswal, the General Secretary of NSSI and the Managing Editor of the Newsletter.

As usual, this Newsletter contains a report on NSSI activities, several highlights on neutron science done in India, and a topical review of a contemporary neutron scattering technique available at Dhruva reactor.

The 13th Asia-Oceania Neutron Scattering Association (AONSA) Neutron School was organized at BARC during November 24-28, 2024. This included 35 distinguished speakers, 110 students and a variety of experiments at the Dhruva reactor. A report from NSSI, as sent to AONSA, is reproduced in this issue.

This issue contains highlights of a broad variety of high-quality neutron science done in India, covering both fundamental and applied aspects. The research areas include unusual hydrogen bonds, magnetism in different compounds, anharmonic phonons, protein and nanoparticle interactions, Li/Na battery materials, and materials science. These highlights emphasize the excellence and breadth of the neutron scattering techniques being pursued by the scientists in India.

The previous issue contained a topical review on conventional small-angle neutron scattering, based on a pin-hole or slit based collimation that enables observation of complex structures of up to ~50 nm scale. Another instrument at the Dhruva reactor is based on an innovative double-crystal collimation that extends this range to ~1000 nm and has been used for very important application over the last 2 decades. The present issue contains a review of this instrument and recent results.

We hope the readers will like this issue and contribute excellent highlights of their research to the future issues.

Published by The General Secretary, NSSI.

Reports as sent to AONSA from NSSI

Organization of 13th Asia-Oceania Neutron Scattering Association (AONSA) Neutron School

Bhabha Atomic Research Centre (BARC) organized the 13th Asia-Oceania Neutron Scattering Association (AONSA) neutron school during November 24-28, 2024 in association with the Neutron Scattering Society of India (NSSI), AONSA, and International Atomic Energy Agency (IAEA), and the Board of Research in Nuclear Sciences (BRNS), Department of Atomic Energy (DAE), Government of India. Dr. S. M. Yusuf, was the Chairman of Organizing Committee with Dr. R. Mittal as School Coordinator, Dr. Anil Jain as Scientific Secretary and Dr. Mala N. Rao as Local Convener.

The AONSA neutron school brought together both the experts as well as young and enthusiastic researchers from various countries in the Asia Oceania region. The present school comprised lectures as well as hands-on experiments covering all important aspects of neutron scattering, including facilities, science and applications. There were a total of 27 speakers from India and 8 from rest of the Asia Oceania region. Mr Joe Mohan, Associate Director Reactor Projects Group, BARC delivered evening talk on “Research Reactors in India: Present and Future”. The lectures of the school were also broadcast on-line to benefit many participants who could not make it to attend the school in-person.

Inaugural session of 13th AONSA Neutron School

The AONSA Neutron School 2024 was attended by 110 Indian participants, and 16 overseas participants [Indonesia (6), Bangladesh (1), South Korea (3), Japan (2), Russia (2), Australia (1), and Poland (1)]. Besides four overseas senior scientists from Japan (2), Australia (1), and IAEA (1) also attended the School as distinguished delegates.

Group Photograph of participants of 13th Asia-Oceania Neutron Scattering Association (AONSA) Neutron School

Photograph taken during the poster session of 13th AONSA Neutron School at BARC, Mumbai

The scientific deliberations, and the scheduled neutron scattering experiments at the Dhruva reactor enriched the participants immensely and is expected to generate several useful collaborations.

S. M. Yusuf
Neutron Scattering Society of India

Highlights of Neutron Research

Deuteration unusually shortens the hydrogen bonds in Bis(glycinium) oxalate: single crystal neutron diffraction

Bis(glycinium) oxalate is a complex of the simplest amino acid glycine and the simplest dicarboxylic acid oxalic acid in 2:1 stoichiometric ratio. Earlier single crystal X-ray and neutron studies had revealed that the complex is held by a very strong O-H…O hydrogen bond between glycinium cation and the oxalic acid dianion, apart from other moderate N-H..O and C-H…O hydrogen bonds. High-pressure Raman, IR and X-ray studies showed that there is a phase transition around 1.7 GPa. To probe further the nature of hydrogen bonds crystals of fully deuterated (FDBGO), C -deuterated (CDBGO) and N deuterated (NDBGO) crystals of BGO were grown. The single crystal neutron diffraction studies were carried out at the four circle single crystal diffractometer at Dhruva [1]. The deuteration level in the case of FDBGO for the strong O-H..O bond was 80% In the case of CDBGO, the hydrogens belonging to C-alpha carbon are fully deuterated and all others are fully hydrogenated. In the case of NDBGO, the hydrogens belonging to C-alpha carbon are hydrogenated, and the hydrogens belonging to nitrogen are around 40% deuterated and 60% hydrogenated, the strong O–H…O bond between the glycinium and oxalate ion is only 25% deuterated. It was found that the O…O donor acceptor distance of the strong O-H..O Hydrogen bond reduced showing inverse Ubbelohde effect. The effect on the other N–H..O hydrogen bonds due to partial substitution of H with D results in shortening of both N–H and N-D covalent distances and also leads to formation of N–H/D…O hydrogen bonds with shorter N…O distances whereas no systematics is observed with the C-H..O bonds. Figure 1 (left) shows the asymmetric unit of FDBGO, CDBGO, and NDBGO and Figure 1 (right) shows the packing in FDBGO.

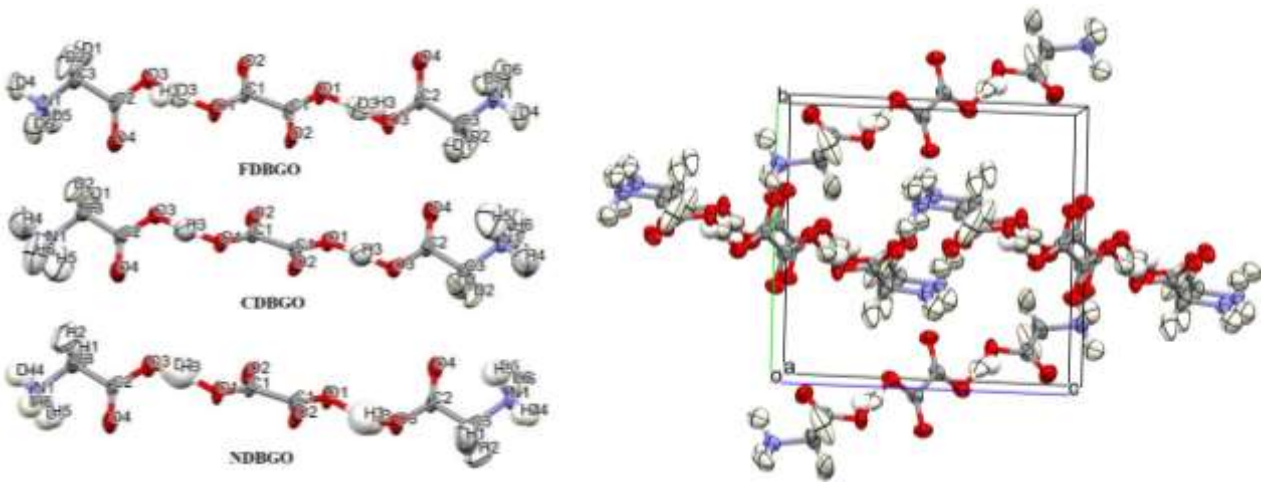

Figure 1. Asymmetric unit of FDBGO, CDBGO, and NDBGO and the packing in FDBGO

1. *Bis(glycinium) oxalate: effect of deuteration, single crystal neutron diffraction and Raman spectroscopic studies*, R. Chitra, R. R. Choudhury, Geogy J. Abraham, Structural Chemistry, https://doi.org/10.1007/s11224-024-02414-1

Contributed by: R. Chitra, BARC, Mumbai (Email: rchitra@barc.gov.in)

Magnetic ground state and spin-Hamiltonian of the spin-5/2 distorted triangular lattice antiferromagnet Na3Fe(PO4)2: Neutron Scattering Investigations

A triangular lattice antiferromagnet is significant in condensed matter physics because it serves as a canonical example of a "geometrically frustrated" system, leading to complex and often exotic magnetic behaviors, including the potential for quantum spin liquid states and rich phase diagrams depending on the specific interactions involved. The compound $Na_3Fe(PO_4)_2$ consists of two dimensional distorted triangular lattice (type-II) of magnetic Fe^{3+} ions. A combined study of neutron diffraction, inelastic neutron scattering (INS), and density-functional-theory (DFT) calculations reveals a collinear antiferromagnetic magnetic ground state and the spin Hamiltonian involving interactions J_1-J_2 confined within the triangular lattice planes [1]. The temperature dependent neutron diffraction patterns reveal magnetic Bragg peaks below ∼11 K, corresponding to a commensurate collinear AFM phase, characterized by $\boldsymbol{k}$ = (1, 0, 0). Such a magnetic state appears due to a strong distortion in the triangular lattice having significantly different NN AFM exchange interactions (J_1/J_2< 0.5) or due to NN exchange interactions with different signs, i.e., FM J_1 and AFM J_2. Our analysis reveals a reduced ordered magnetic value of 3.77(6) μ_B/Fe^{3+} at 6 K. The powder INS spectrum consists of two bands of magnetic excitations (over 0.25–2.0 and 3.0–5.5 meV) with a small energy gap of ∼0.25 meV, a typical characteristic feature of spin-wave excitations of an ordered magnetic state. We model the experimentally observed features of magnetic excitations by linear spin-wave theory and determine the dominant in-plane magnetic exchange interactions J_1 = −0.31 meV (FM), and J_2 = 0.15 meV (AFM). The values of the exchange interaction constants determined from the INS study and the DFT calculations are in good agreement. Further, the interplanar exchange interaction [J_3 = 0.00003 meV (AFM)] has been estimated to be negligible. Present study provides a benchmark for a quantitative description of the magnetic properties of distorted triangular lattice antiferromagnet.

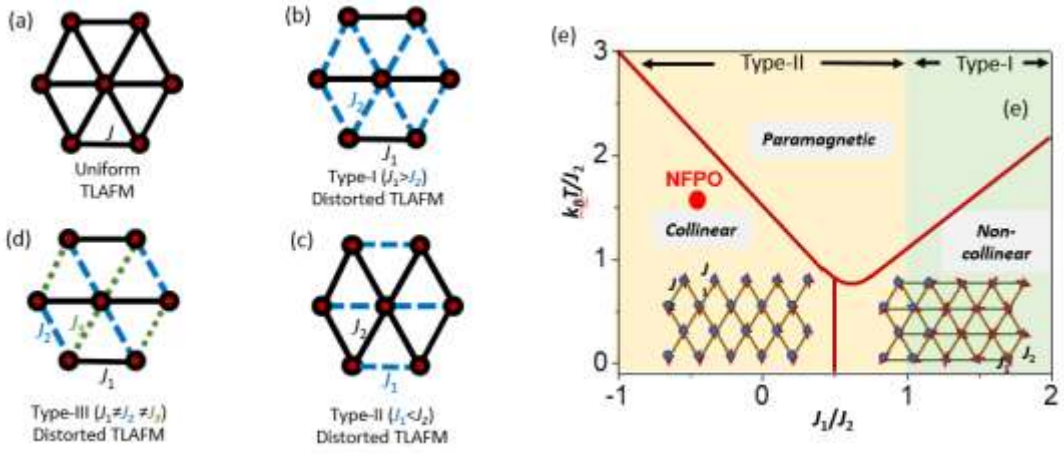

Figure. (a) Figure: Variety of 2D triangular lattices, viz., (a) isotropic triangular lattice (with uniform exchange interactions J), and distorted triangular lattices of (b) type-I ($J_1 > J_2$), (c) type-II ($J_1 < J_2$) and (d) type-III ($J_1 \neq J_2 \neq J_3$). (e) Magnetic phase diagram for isosceles distorted triangular lattice [type-I ($J_1 > J_2$) and type-II ($J_1 < J_2$)]. The position of the present compound NFPO is shown by solid circle.

1. *Magnetic Excitations and Spin-Hamiltonian of the Spin-5/2 Distorted Triangular Lattice Antiferromagnet $Na_3Fe(PO_4)_2$,* B. Saha, A. K. Bera, S. M. Yusuf, R. Roy, S. Kanungo, D. Le and A. Krajewskam, Phys. Rev. B 110, 094421 (2024).

Contributed by: A.K. Bera, BARC, Mumbai (Email: akbera@barc.gov.in)

Stabilization of ferromagnetism in $CaRuO_3$:
A Neutron Diffraction and Neutron Depolarization Study

Perovskite oxides are renowned for their diverse magnetic ground states, arising from the interplay of electron-electron interactions, spin-orbit coupling (SOC), and crystal field (CF) effects. Among these, $CaRuO_3$ is intriguing as it lies near a quantum critical point and yields no magnetic long-range ordering, making its magnetic behavior highly sensitive to external perturbations such as chemical doping. In this study, 15% Cr doping in CaRuO3 (CRCO15) is shown to induce ferromagnetic (FM) order below 100 K. Temperature-dependent neutron powder diffraction (NPD) [using the PD-1 diffractometer, BARC], neutron depolarization [using the PNS, BARC] measurements were employed to unravel the origin of magnetism in CRCO15.

The analyses of the NPD patterns [Fig.1 (a) and (b)] suggests orthorhombic crystal structure with *Pnma* space group symmetry for both the compounds CRO and CRCO15. However, our NPD study reveal that the Cr-substitution introduces octahedral tilt (ϑ) and stretching distortions, alongside a reduction in the orthorhombicity factor and unit cell volume [Fig. 1]. The temperature dependent crystal structural parameters of CRCO15 correlate strongly with magnetic ordering at T_C=100 K, in agreement with the magnetization data. Interestingly, no magnetic Bragg peaks were detected for CRCO15, likely due to the low value of the ordered magnetic moment below the detection threshold (< 0.4 μ_B/f.u.). Nevertheless, the FM ordering in CRCO15 has been confirmed by neutron depolarization study [Fig. 1(e)]. Structural modulations (such as lattice parameter, volume, and octahedral distortions) near T_C=100 K were observed in CRCO15 but absent in CRO, highlighting the role of Cr doping in stabilizing FM order.

This study demonstrates that modest Cr doping effectively transforms the spin-disordered ground state of CRO into a ferromagnetic phase by inducing temperature-dependent structural modulations, establishing a strong correlation between crystal structure and magnetic properties.

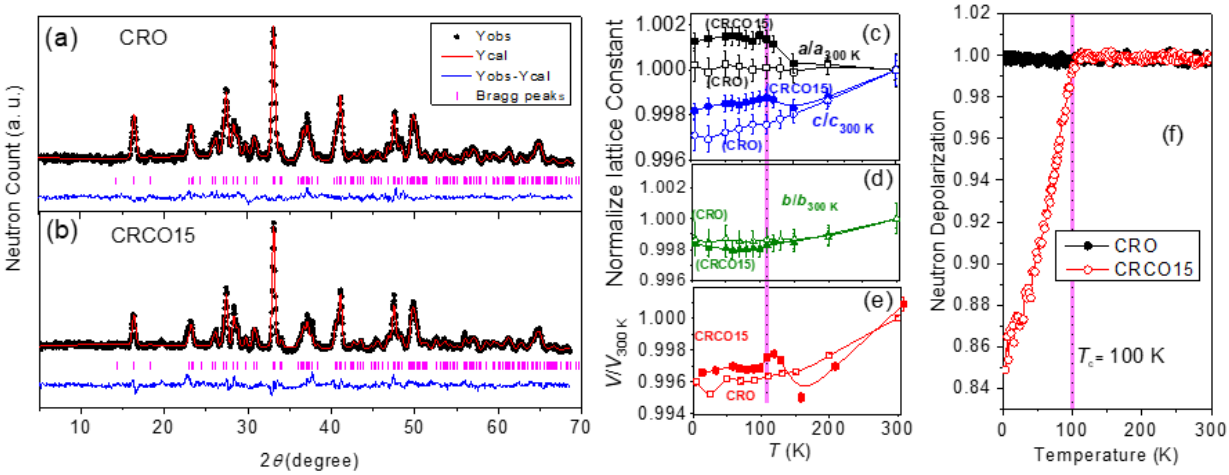

Figure 1. (a-b) Measured and calculated diffraction patterns for CRO and CRCO15 compounds at room temperature. (c-e) Temperature dependence of the normalized lattice parameters, unit cell volume, and neutron beam depolarization, respectively, for both the compounds

1. Stabilization of ferromagnetism via structural modulations in Cr-doped $CaRuO_3$: A neutron diffraction and Raman spectroscopy study, Pooja, K. S. Chikara, Aprajita, S. N. Sarangi, D. Samal, S. Saha, A. K. Bera, S. M. Yusuf, and C. Sow, Physical Review B 110, 184425 (2024).

Contributed by: A.K. Bera, BARC, Mumbai (Email: akbera@barc.gov.in)

Unraveling intricate magnetic behavior involving negative magnetization, spin reorientation, and exchange-bias in $ErFe_{0.5}Co_{0.5}O_3$

Orthoferrites, $RFeO_3$ (R = magnetic rare-earth) compounds exhibit intriguing magnetic properties, such as negative magnetization (NM), exchange-bias (EB) and spin-reorientation (SR). A correlation among these magnetic properties has not been explored in orthoferrite compounds. By replacing Fe^{3+} with non-magnetic Co^{3+} in $RFeO_3$ (R = Er), Fe-Fe and R-Fe superexchange can be tuned and it may give rise to intriguing and complex magnetism in the $ErFe_{0.5}Co_{0.5}O_3$ (EFCO) compound. A comprehensive neutron diffraction study involving distinctive magnetic behaviors of NM, EB, and SR has been carried out in the EFCO compound [Fig. 1].

The DC magnetization study indicates the presence of the NM phenomenon in the compound, with a compensation temperature (T_{COMP}) of 24 K. Neutron diffraction study over 1.5–300 K elucidates the spin reorientation (SR) of Fe/Co spins at 100 K (T_{SR}) and Er magnetic ordering <4 K (T_N^{Er}) resulting in $\Gamma_4(G_x)$, $\Gamma_{24}(G_z,G_x)$, $\Gamma_2(G_z)$, and $\Gamma_{257}(Gz;A_y^{Er}G_z^{Er})$ magnetic structures at $T > T_{SR}$, $T_{SR} \geq T > T_{COMP}$, $T_N^{Er} < T \leq T_{COMP}$, and $T \leq T_N^{Er}$, respectively. For $T > T_N^{Er}$, the Er moment (M_{Er}) becomes polarized under the internal field generated by the ordered Fe/Co moments. This polarization of the Er moment is evidenced by the Schottky anomaly observed in the specific heat data and the monotonic increase in AC susceptibility below the T_{COMP}. The observed negative magnetization in the compound is explained using Cooke's model, where M_{Er} competes with the weak ferromagnetic (FM) component ($M_{Fe/Co}$) arising from the canted antiferromagnetic (AFM) ordering of Fe/Co moments. As per Cooke's model, the negative internal magnetic field aligns M_{Er} opposite to both $M_{Fe/Co}$ and the applied magnetic field below the T_{COMP}, thereby bringing the compound to a NM state.

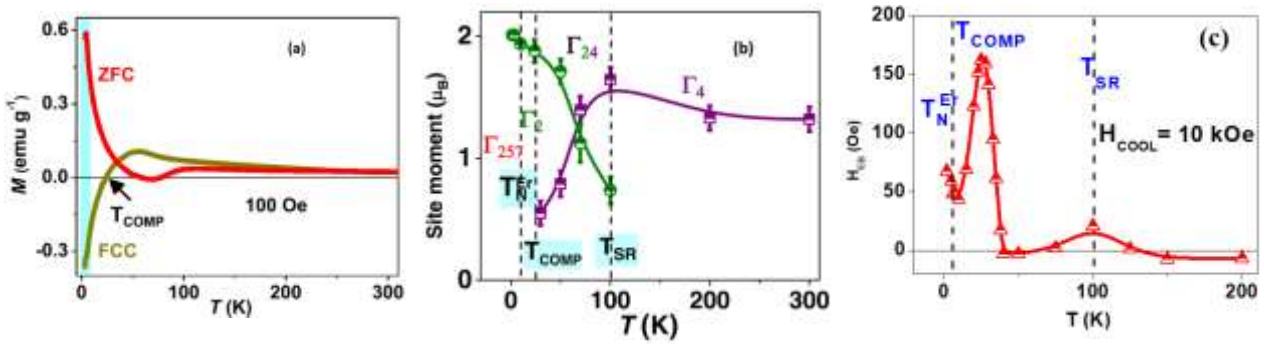

Fig. 1: (a) DC magnetization study showing negative magnetization in $ErFe_{0.5}Co_{0.5}O_3$. (b) Derived site magnetic moments as a function of temperature highlighting the regions of Er ordering (T_N^{Er}), compensation temperature (T_{COMP}), and spin-reorientation (T_{SR}). (c) Exchange-bias (H_{EB}) behaviour in different temperature regions showing anomalies at T_N^{Er}, T_{COMP}, and T_{SR}.

The EB shows anomalous behavior with a maximum positive value at the T_{COMP}, and its behavior is linked to spin arrangement changes as a function of temperature. The pivotal role of Er and Fe/Co exchange coupling in shaping the intriguing and complex magnetic properties has been provided.

1. *Unraveling intricate magnetic behavior involving negative magnetization and exchange-bias in in $ErFe_{0.5}Co_{0.5}O_3$,* D. Garg, A. Kumar, S. M. Yusuf, Phys. Rev. B **110**, 104401 (2024).

Contributed by: Amit Kumar, BARC, Mumbai (Email: amitkr@barc.gov.in)

Powder neutron diffraction studies on quaternary Heusler alloy CuNiCrAl

The influence of atomic structure on the magneto-transport characteristics of the new quaternary Heusler alloy CuNiCrAl has been investigated. Nuclear structure studied through X-ray diffraction indicates the presence of mixed phase of cubic and tetragonal with the ratio of 67:33. Due to similar atomic scattering factor of the constituent elements Cu, Ni, Cr and Al, some of the peaks like (111) and (200) peaks typically observed in a well ordered Heusler alloy can be missed in X-ray diffraction. Therefore, Neutron diffraction has been conducted using a powder diffractometer (PD-3) to validate the X-ray results. It possesses an advantage over XRD due to the varying scattering lengths of neutrons from the constituent elements (bCu = 7.718 fm, bNi = 10.3 fm, and bCr = 3.635 fm). Refinement of neutron diffraction revealed that the cubic to tetragonal ratio is 90.9:7.3. The influence of B2 disorder (indicated by presence of (200) reflection) and the coexistence of cubic and tetragonal phases on various magnetic and transport properties has been further examined. The magnetization data indicate the occurrence of a Griffith's-like phase along with the fully compensated ferrimagnetic state coexist with other magnetic ordering at low temperatures. Due to presence of mixed nuclear and magnetic phase asymmetric behaviour of magnetoresistance is detected which implies the presence of spin valve like effect in this system.

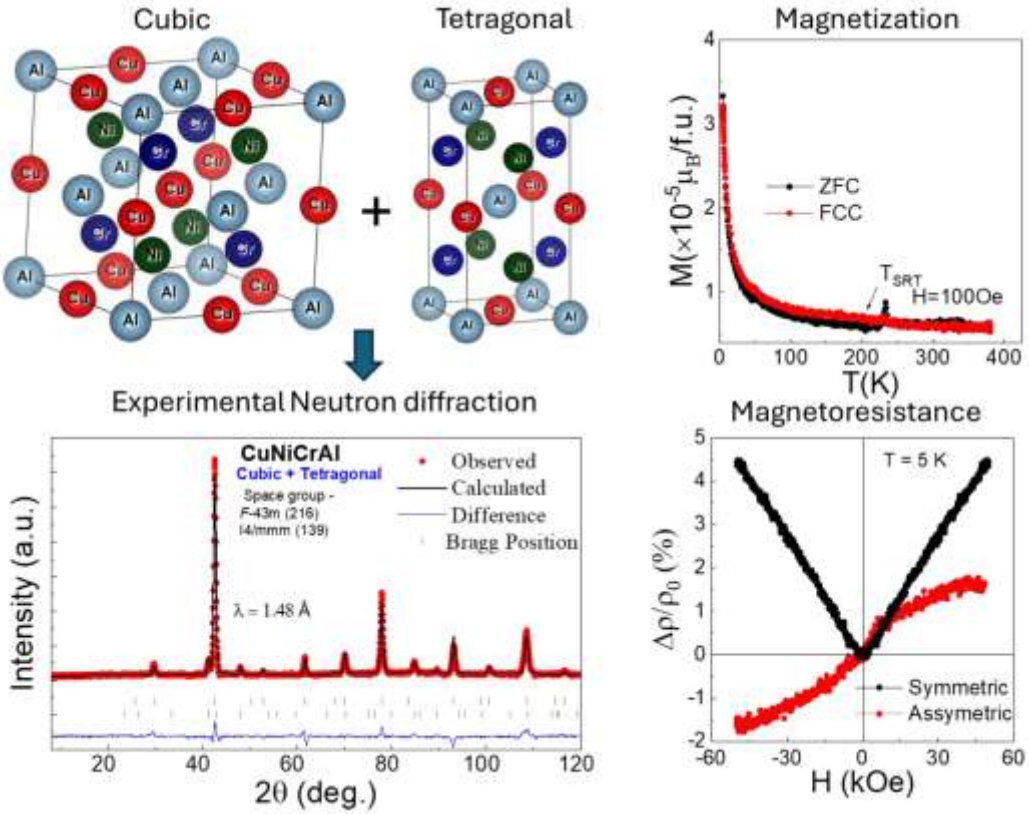

1. *Griffiths phase-like behavior with compensated ferrimagnetism and spin valve effect in quaternary Heusler alloy CuNiCrAl,* Surbhi Gupta, Akhilesh Kumar Patel, Sudip Mukherjee, P.D. Babu, S.D. Kaushik, Nirat Ray and K.G. Suresh, journal of Alloys and Compounds **1010,** 177836 (2025).

Contributed by: Surbhi Gupta, IIT Delhi (Email: surbhi199015@gmail.com)

Examining novel double perovskite $Pr_3Ni_2NbO_9$ through powder neutron diffraction

Perovskites (ABO_3), the all-time interesting class of compounds has grabbed significant attention of material science research group as they offer promising physical properties along with exciting and crystal structure. The strong structure correlations with the properties and the chemical flexibility provided by the choice of suitable ions at A and B sites enhance the beauty of these compounds. Several compounds by optimizing elements at A and B site in single (ABO_3) and double perovskite ($A_2B_2O_6$/ $A_2BB'O_6$) format have been reported previously. In double perovskite two different elements can be chosen in 1:1 ratio. Here we have synthesised novel double perovskite compound where the elements at B site were chosen to 2:1 ratio (i.e. $A_2B_{2/3}B'_{1/3}O_6$) which lead to modified double perovskite format thus offering 2+ and 5+ valance element to be accommodated in double perovskite format as our goal in tailoring physical properties.

The room temperature x-ray depicted the structure of modified double perovskite $Pr_3Ni_2NbO_9$ to be in monoclinic (P 21/n) phase. Neutron diffraction played a significant role in affirming absence of secondary phases. The temperature dependent magnetization measurements showed antiferromagnetic like interactions in the title compound. To obtain the clear magnetic structure a detailed temperature dependent neutron diffraction was performed using PD-3 diffractometer, though within the q range and resolution of diffractometer we were not able to see signature of long-range ordering. This observation was further confirmed by field dependent heat capacity measurements. The absence of long-range ordering may be attributed to random distribution of Ni2+ and Nb5+ ions at 2d site, which may lead to fluctuation of magnetic domain at local level, due to this cation ordering may be present only at local level not at global level, thus long-range order is missed.

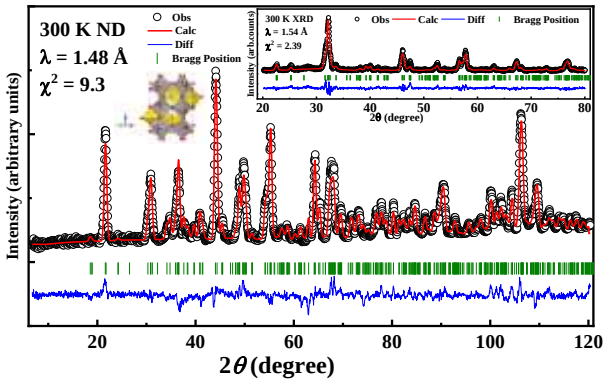

Neutron diffraction pattern of $Pr_3Ni_2NbO_9$ at 300 K.

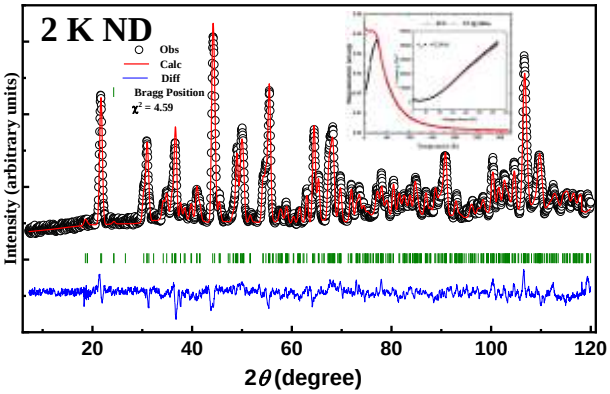

Neutron diffraction pattern of $Pr_3Ni_2NbO_9$ at 2 K**.**

1. *Synthesis, structure and magnetic properties of $Pr_3Ni_2NbO_9$ double perovskite,* R. Athira, Yogesh Kumar, DP Sahu, AK Singh, RJ Choudhary, S. D. Kaushik, Ceramics International **51**, 8758 (2024)

Contributed by: S.D. Kaushik, UGC-DAE CSR, Mumbai Centre (Email: sdkaushik@csr.res.in)

Complimenting Magnetic Properties of A_2MnTiO_6 (A = Ca, Ba) using Powder Neutron Diffraction

Materials having perovskite structures have been important for a number of reasons. In double perovskites of the A_2MXO_6 type, A is divalent ion especially an alkaline earth metal, and M & X are tetravalent transition metal ions which may or may not be magnetic, are interesting class of compounds to study. This class of materials have exciting characteristics like ionic conductivity, magnetoresistance, multiferroicity, exotic magnetism, and thermoelectric figure of merit.

We have used temperature dependent neutron powder diffraction to complement the magnetic properties of the compounds Ca_2MnTiO_6 and Ba_2MnTiO_6. The Ca compound forms in an orthorhombic structure whereas the Ba compound forms in a rhombohedral structure. Among the compound's interesting magnetic susceptibility behaviour's is magnetization reversal, which is defined as negative magnetic susceptibility at low applied fields that becomes positive at higher fields for the Ca compound. The magnetic frustration parameter, f, for this compound is also very high (≥ 10). In addition, there are two anomalies in magnetic susceptibility that surround T_{N1} at 8.2 K and T_{N2} at 121–124 K. In Ba_2MnTiO_6 sample, magnetization studies indicate a highly frustrated magnetic ground state ($f > 10$) and antiferromagnetic ordering around 45 K, but no long-range magnetic order.

Neutron powder diffraction measurements were carried out for both the compounds and have been analyzed using Rietveld refinement method, for data measured between 3 K and 300 K. For both samples, no new Bragg peaks appeared down to 3 K, and the neither did we observe broadening of the Bragg peaks or a hump kind of feature which rules of any kind of long-range magnetic ordering, while indicating that both compounds can be strong candidates for compounds exhibiting Quantum Spin Liquid kind of features. Neutron diffraction results thus clearly supports the magnetization data, which confirms the highly frustrated magnetic ground states in both the compounds.

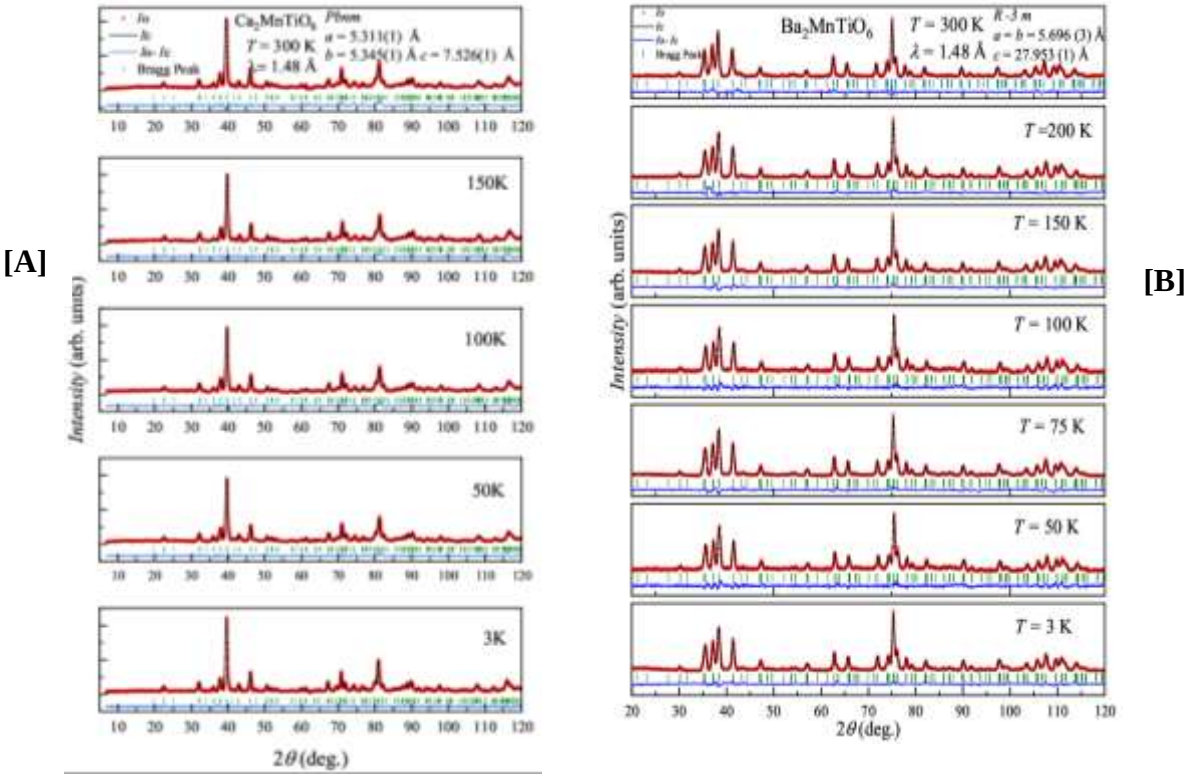

Fig. Temperature dependent neutron diffraction profiles for [A] Ca_2MnTiO_6 and [B] Ba_2MnTiO_6, measured on PD-3 at Dhruva reactor (Trombay) using CCR based cryostat, are shown here with analysis carried out using Rietveld refinement method.

1. *Structural and magnetic properties of mixed valent Ca2MnTiO6*, Smita Borole, Soumen Samanta, Shovit Bhattacharya, Sudhindra Rayaprol, J. Magn. Magn. Mater. **605** (2024) 17328

Contributed by: S. Rayaprol, UGC-DAE CSR, Mumbai Centre (email: sudhindra@csr.res.in)

Structure and Magnetism of the Mixed Valent Compound, $CeFe_2Al_8$

The structural and magnetic properties of orthorhombic (space group: *Pbam*) $CeFe_2Al_8$ investigated through experimental studies, that is, powder neutron diffraction, bulk magnetization and X-Ray photoemission spectra reveal mixed valence of Ce and highly frustrated magnetic ground state. Low-field *dc* magnetization measurements reveal an antiferromagnetic ordering with a Néel temperature (T_N) around 4 K. The magnetic susceptibility shows a broad hump across a wide temperature range, indicating a mixed valence state of Ce, which is consistent with previously reported literature and further confirmed through XPS measurements as the XPS studies clearly indicate the mixed valence (3^+ and 4^+) of cerium in $CeFe_2Al_8$. However, contrary to earlier findings, we observe that the mixed valence state (broad hump in susceptibility) persists even under high magnetic fields (> 2T). The Fe magnetic moments compete with cerium moments, leading to a dilution of long-range magnetic order and contributing to magnetic frustration in $CeFe_2Al_8$. The magnetic frustration parameter, f > 15 clearly indicates frustrated magnetic ground state, akin to Quantum Spin Liquid systems. The observed non-saturating and non-linear magnetization curves with respect to ramping fields suggest the presence of weak magnetic order at low temperatures.

Powder neutron diffraction profile of $CeFe_2Al_8$ measured at 3K and analysed using Rietveld refinement method indicate that this compound does not show any changes in the nuclear structure and in the absence of the clear magnetic Bragg peak, long range magnetic order is found to be absent in this compound at this temperature. Thus, bulk magnetization and nuclear diffraction experiments can help in understanding the correlation between structural and physical properties.

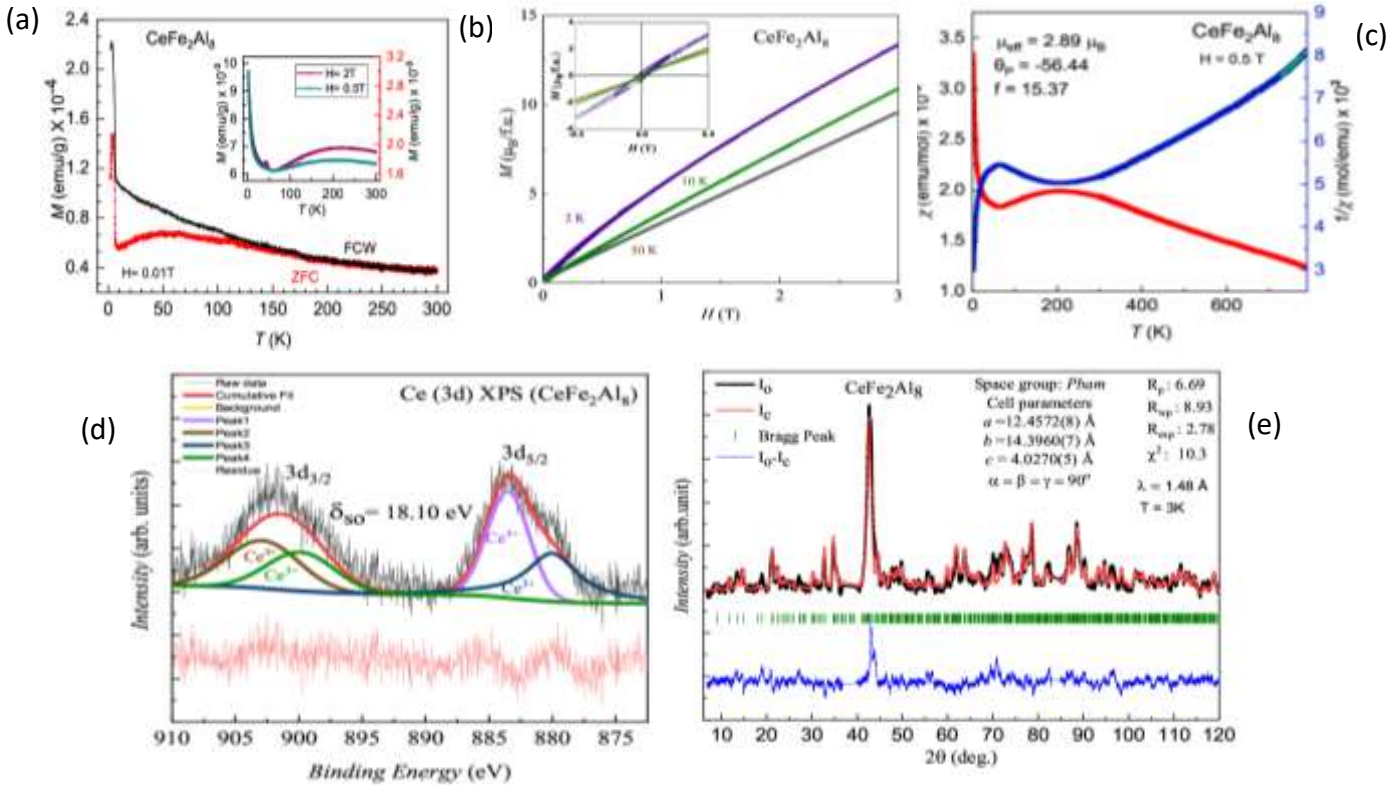

Figure. (a) Susceptibility in ZFC and FCW state of $CeFe_2Al_8$ sample measured under H = 0.01T. The inset shows the M vs. T at H = 0.5T and 2T. (b) The magnetization plot for the $CeFe_2Al_8$ at different temperatures and fields. (c) High temperature magnetic susceptibility (χ vs. T) of $CeFe_2Al_8$. (d) The deconvoluted XPS data of cerium fits into $3d_{5/2}$ & $3d_{3/2}$ peaks with valence states $Ce4^+$ & $Ce3^+$ (e) Neutron powder diffraction data at T = 3K, analysed using Rietveld refinement method.

1. *Structure and properties of mixed valent CeFe2Al8*, Nilofar Kurawle, Soumen Samanta, Shovit Bhattacharya, and Sudhindra Rayaprol, J. Phys.: Cond. Matt. 37, 025606 (2025).

Contributed by: S. Rayaprol, UGC-DAE CSR, Mumbai Centre (email: sudhindra@csr.res.in)

Anharmonic Phonons and Anomalous Thermal Expansion in Vanadium Metal

Vanadium is the sixth most abundant among transition metals. From an application point of view, it is the most demanding and essential metal in the alloy and steel industry. Interestingly, vanadium exhibits anomalous thermal expansion behaviour at high temperatures. Strong phonon anharmonicity at elevated temperatures leads to unusually large lattice expansion. Using neutron inelastic scattering measurement at DHRUVA, Trombay (Figure (a)) and advanced simulations, we have extensively identified the role of phonons in the anomalous thermal expansion behaviour of vanadium, particularly at high temperatures. We compared the different methods to evaluate the phonon anharmonicity, namely, the quasiharmonic approximation (QHA), and machine-learned force-field-based molecular dynamics (MLMD) simulations. At higher temperatures, the experimental thermal expansion coefficient continues to rise up to twice the QHA estimates, indicating significant anharmonicity. The MLMD, which includes all the anharmonic effects, successfully explained the anomalous expansion behaviour over 500-2000 K (shown in figure (c)). We used MLMD to calculate the spectral energy density of phonons up to 2000 K which reveal small phonon shifts but large broadening (shown in figure (b)). We compared this SED plots with the harmonic phonon dispersion as well as available measurement at 300K.We have highlighted the limitation of quasi-harmonic approximations (QHA) to predict the high-temperature thermal expansion behaviour in such a strongly anharmonic system. The MLMD force-field was validated by computing the phonon density of states using MLMD-forcefield and compared with measured phonon density of states using inelastic neutron scattering at Triple Axis Spectrometer, DHRUVA, Trombay (Figure (a)). Other available results from neutron and X-ray inelastic scattering experiments were also used to validate the simulations (Figure 1(b)).

The MLMD simulation reproduces the experimental thermal expansion data quite well, it appears that the thermal expansion is largely dominated by the phonon contributions. The MLMD results bring out the important and essential role of the fourth- and higher-orders of phonon anharmonicity in thermal expansion of vanadium.

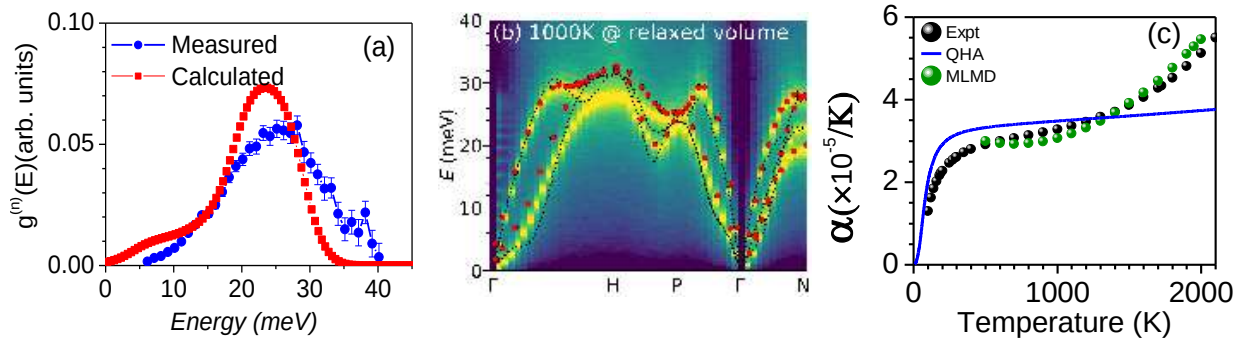

Figure: (a) The calculated thermal expansion coefficient of vanadium using QHA and MLMD simulations, compared with the available measurements (Y. M. Kozlovskii et. al, J. Phys.: Conf. Ser. 1677, 012167 (2020)), (b) The calculated truly anharmonic phonon dispersions at 1500K from MLMD simulations were compared with the available measurements at 300K (red circle) (A. Bosak et. al, Phys. Rev. B 78, 020301(R) (2008)) and harmonic phonon dispersion (black dot lines), highlights the phonon broadening and shifting effect. (c) The measured phonon density of states using inelastic neutron scattering experiments are used to bench mark the simulations.

1. *Untangling high-temperature thermal expansion and lattice thermal conductivity behavior of vanadium using machine-learned molecular dynamics*, S Malgope, M K Gupta, S Bag, R Mittal et al. Phys. Rev. B **110**, 054301 (2024).

Contributed by: M.K. Gupta, BARC, Mumbai (Email: mayankg@barc.gov.in)

An Interplay Between Zwitterionic Surfactants and Pluronics

Zwitterionic surfactants, specifically dodecyl dimethyl(3-sulfopropyl) ammonium hydroxide inner salt (SB3−12) and 3-(myristyldimethylammonio) propanesulfonate (SB3−14), were incorporated into pluronics (F127 and F108), resulting in a unique formulation in aqueous medium [1]. These surfactants, known for their amphoteric biodegradable nature, present a greener alternative for surfactant systems.

An in-depth investigation into the photophysical properties of the twisted intramolecular charge transfer (TICT) active probe, trans-2-[(4-dimethylamino) styryl] benzothiazole (DMASBT), has unveiled key insights into the interactions between zwitterionic surfactants and pluronics. Excited-state behavior of the DMASBT probe revealed an increase in polarity with a predominant micro viscous microenvironment, as evidenced by steady-state and time-resolved fluorescence emission studies. Dynamic light scattering techniques, shows the reduced size of pluronic micelles in the presence of zwitterionic surfactants.

Structural validation using small-angle neutron scattering (SANS) along with fluorescence lifetime imaging microscopy (FLIM) and cryogenic transmission electron microscopy (Cryo-TEM) confirmed the spherical morphology and compact size of these micelles. The spatial proximity between atoms in this zwitterionic surfactants-pluronic systems was further supported by nuclear Overhauser effect spectroscopy (NOESY). Comparison of SANS parameters between different systems is illustrated in Figure 1. This fundamental investigation into the photophysical properties and microenvironmental features of zwitterionic surfactant-pluronic mixed assemblies holds significant promise for future applications in pharmaceuticals, cosmetics, and targeted drug delivery.

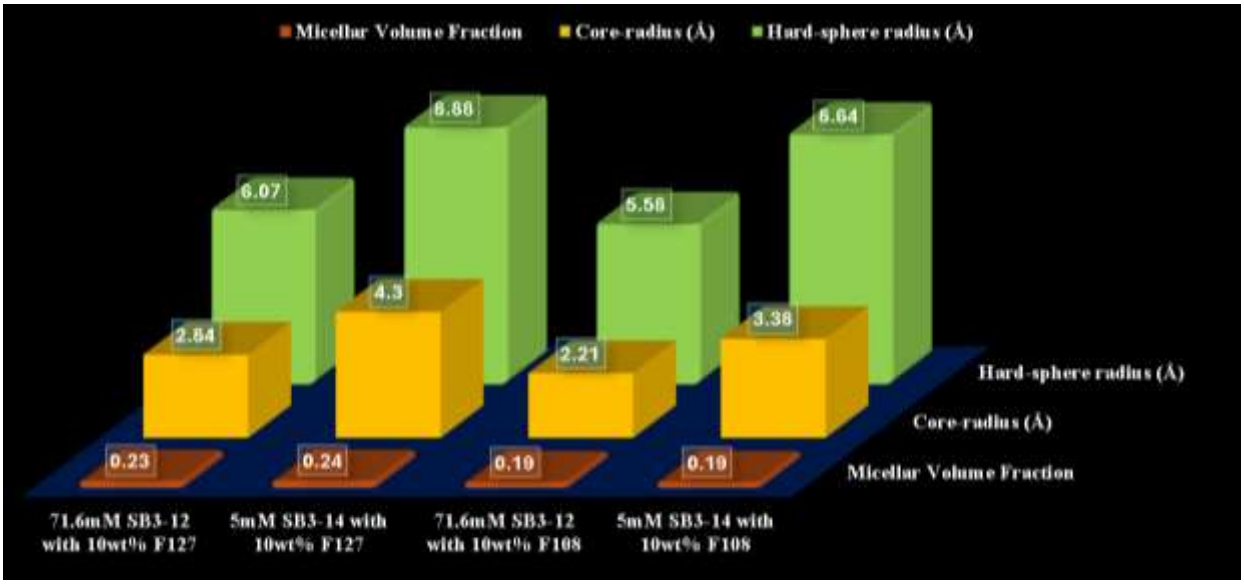

Figure 1: The hard sphere radius, core-radius, and micellar volume fraction with their corresponding values in various systems – 71.6mM SB3-12 with 10wt% F127, 5mM SB3-14 with 10wt% F127, 71.6mM SB3-12 with 10wt% F108 and 5mM SB3-14 with 10wt% F108 as obtained using SANS are shown through column plots.

1. Deciphering the Influence of Zwitterionic Surfactants on Pluronic Co-assemblies: A Synergistic Odyssey through Spectroscopic, Microscopic, and Scattering Techniques. S. Sinha, S. Srivastava, V. K. Aswal, and D. Seth, Langmuir, **40**, 24419, (2024).

Contributed by: D. Seth, IIT Patna (Email: debabrata@iitp.ac.in)

Conformational Behavior of HSA Protein Induced by Surface-Active Ionic Liquids

The interaction of Human Serum Albumin (HSA) protein with surface-active ionic liquids (SAILs) with (1-decyl-3-methylimidazolium bromide (DIB), 1-dodecyl-3-methylimidazolium bromide (DDIB) have been examined using Small-angle neutron scattering. The two SAILs have same head groups (imidazolium) but differ in chain length, the later carrying two more carbons than former.

Figure 1 presents SANS data of 2 wt% HSA without and with DIB (Figure 1a) and DDIB (Figure 1b) across premicellar, micellar, and postmicellar concentration ranges. In buffer, pure HAS dispersion exhibits a monotonous decrease in scattering intensity, indicating negligible interparticle interactions (S(Q)~1). The data is modeled using an oblate ellipsoidal structure with semimajor and semiminor axes of 4.0 nm and 1.4 nm, respectively. In the presence of DIB, only minor changes in scattering were observed, particularly in the low-Q region. The data of HAS + DIB system is similarly fitted using the oblate ellipsoidal model. A slight increase in protein size is observed, suggesting partial interaction between two components, where monomers attach to the native protein structure without full unfolding. Conversely, the addition of DDIB induces significant changes in the scattering profile. At premicellar concentrations, the data align with the oblate ellipsoidal model for HSA. However, at micellar and higher concentrations, SANS data reveal linearity in the intermediate Q-range on a log–log scale, characterized by two Q cut-offs. These features indicate a bead-necklace structure, suggesting complete protein unfolding. At these concentrations, DDIB forms micelle-like clusters around the hydrophobic regions of the unfolded protein.

The study suggests significant role of alkyl chain length in SAIL-induced unfolding of the protein.

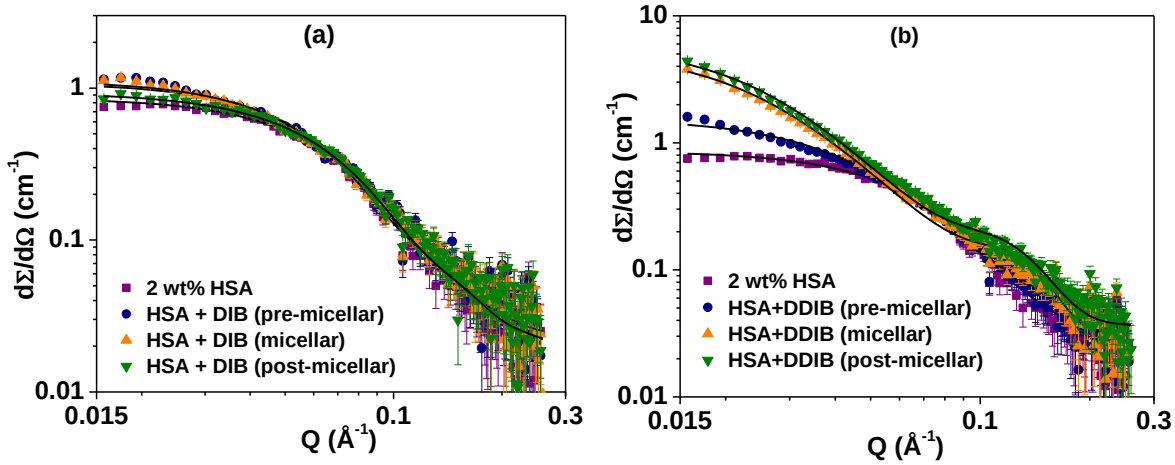

Figure 1. The SANS scattering profiles HSA in the absence and presence of varying concentrations of DIB (Figure a) and DDIB (Figure b).

Ref. *Molecular Insights into the Conformational and Binding Behaviors of Human Serum Albumin Induced by Surface-Active Ionic Liquids*, D. Ray, D. Chamlagai, Sugam Kumar, S. Mukhopadhyay, S. Chakrabarty, V. K. Aswal and S. Mitra, J. Phys. Chem. B **128**, 6622 (2024).

Contributed by: S. Mitra, NEHU, Shillong (Email: smitranehu@gmail.com)

Small-Angle Neutron Scattering reveals the structural details behind enhanced storage performance of low-cost hard carbon derived from biomass

Although sodium-ion battery is still in its early developmental stage, it has gained significant attention as a potential substitute for Lithium-ion batteries (LIB), particularly for low value electric vehicles, such as 2/ 3-wheelers and large-scale stationary storage applications. This is primarily due to abundance of sodium compounds and its similar working principles to LIB. While graphite anode is most widely used as anode material for Li-ion batteries, non-graphitizable carbon, known as 'hard carbon' (HC) is the best choice as anode material for Na-ion batteries. HC is typically obtained through carbonization process, such as thermal or chemical treatment of pure organic compounds or biomass-derived precursors. During such a carbonization process, volatile moieties, such as H_2O, CO_2, CO, N_2 and NO_x are released causing high porosity, low particle density and bulk powder density, while retaining the original micro-morphology of the starting precursor materials. In a recent work [1], HC anode materials were derived from biomass precursors, sugarcane waste (DB1400) and corn waste (DC1400), and compared their performances (storage capacity of DB1400: ~307 mAh/g) with commercially available (storage capacity: ~275 mAh/g) hard carbon (Type C). The voltage profile during insertion of Na-ions and electrons into HC usually exhibits sloppy region due to adsorption of Na on the HC surfaces followed by plateau region associated with storage within the HC bulk. It is highly desirable to achieve long plateau region as compared to the sloppy region of the voltage profile in order to achieve lower Na insertion potential close to 0.1V for the HC for enhancing the energy density of sodium-ion batteries. Hence, control of the open and closed pores of the HC micromorphology during synthesis processes becomes crucial. DB1400 HC showed higher capacity in plateau (~73%) than slope (~27%) region, while Type C HC displayed storage capacity of ~56% and ~44% in plateau and slope regions respectively. Small Angle neutron Scattering (SANS), which includes the data from two SANS facilities at Dhruva reactor, revealed that correlated graphitic domains, with hexagonal ordering along with fractal like agglomeration of the nanosheets, are responsible for higher plateau capacity of the HC from sugarcane waste.

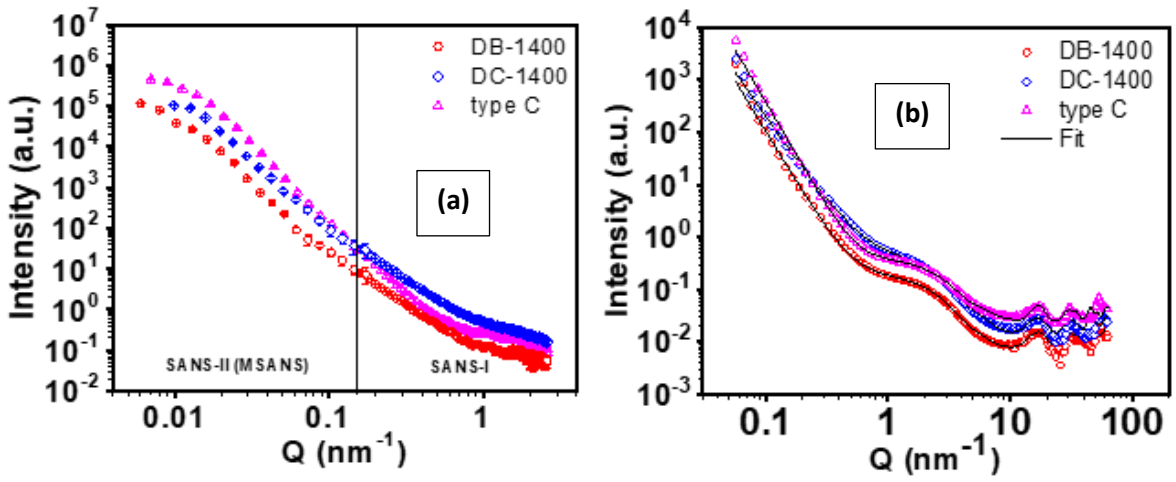

Figure 1. (a) Combined SANS profiles from two facilities at Dhruva reactors and (b) SANS profile from TAIKAN, J-PARC.

1. *Enhanced storage performance of a low-cost hard carbon derived from biomass*, C. Wang, D. Sen, V.K. Aswal, L. Weiguang and P. Balaya, Carbon Trends **17**, 100415 (2024).

Contributed by: P. Balaya, NUS, Singapore (Email: mpepb@nus.edu.sg)

A short status review on a Neutron Technique

Quantifying Mesoscopic Structures in Materials: Insight from Small-Angle Neutron Scattering Experiments using Double-Crystal Based Facility at Dhruva

Avik Das[a], Jitendra Bahadur[a,b], Debasis Sen[a,b*]

[a]*Solid State Physics Division, Bhabha Atomic Research Centre, Mumbai 400085*
&
[b]*Homi Bhabha National Institute, Anushaktinagar, Mumbai 400094*
*Email: debasis@barc.gov.in

Abstract

Small-Angle Neutron Scattering (SANS) is an important non-destructive technique that provides quantitative structural information about various density fluctuations in materials, over a length-scale ranging from typically from 1 to 1000 nanometer. Such mesoscopic inhomogeneities, that govern many crucial physicochemical properties of materials, are ubiquitous in the purview of condensed matter. These inhomogeneities include precipitates in alloys, colloids, nano-particles, membranes, polymers, micelles, pores in porous media. In a unique way, this non-destructive technique opens the door to "nanocosmos", and it allows quantitative analysis in a statistically averaged fashion. In fact, this technique has become indispensable in every domain of science and technology. In the last issue of NSSI Neutron Newsletter, a review on the technique of SANS, using conventional SANS facility (SANS-I) at Dhruva reactor, was illustrated. However, owing to practical constraints, accessing inhomogeneity size larger than typically 50 nm becomes challenging using a conventional pinhole/slit collimation-based SANS facility. Double crystal-based SANS facilities can overcome this limitation.

In this article, the basic principle of double crystal-based SANS along with some recent examples based on the work utilizing MSANS facilities at Dhruva reactor, Bhabha Atomic Research Centre, Mumbai.

1. Introduction

The indispensability of the small-angle neutron scattering (SANS) is increasingly realized as its applications in different domains of science and technology has grown leaps and bounds, particularly in last two decades. In general, conventional slit-collimation based SANS instruments, equipped with 2-D/1-D position sensitive detectors, are widely used for investigating structures in materials, particularly in soft matter & biological materials. In the last issue of NSSI Neutron Newsletter, a review on the technique of SANS using conventional SANS facility (SANS-I) at Dhruva reactor was illustrated. It may be noted from the review that the typical maximum accessible length scale for a slit-collimation instrument is typically 50-100 nm. This constraint arises primarily due to finite beam size, finite beam divergence, necessity arising due to compromising between resolution and available neutron flux, gravity effect of neutrons for large sample to detector distance etc. However, larger inhomogeneities, as commonly encountered in various functional materials including granular materials, cements, ceramics, macro-molecules, magnetic domains etc. are sometimes beyond the resolution limit of the conventional slit-collimation instrument.

To access such larger length scales, double-crystal (DC) based instrument with non-dispersive (1,-1) setting is used and this is known as Bonse and Hart configuration. The sample is placed between the two crystals, and the scattering profiles of the specimens are recorded by rotating the second crystal. In a double-crystal based instrument, unlike slit-collimation instrument, the collimation is performed in the reciprocal space only and the resolution in wave-vector transfer q is independent of the beam cross section. Because of the non-dispersive setting of both the crystals,

the width of the rocking curve is independent of the divergence of the incoming beam. The high q-resolution exists in one dimension only and slit corrections have to be applied to the recorded data. The instruments are compact and do not require 2D-position sensitive detector and long flight paths.

However, due to the necessity of recording of scattering intensity through a step-by-step rotation of the analyser crystal, measurement time is rather long. Further, the sensitivity of the instrument is poor at high *q* vis-à-vis slit collimation instrument, due to a background caused by diffuse scattering from the crystal surfaces. There are a few of double-crystal based small-angle neutron/X-ray scattering facility around the world [1, 2].

In this article, the indigenously developed double-crystal based medium resolution small-angle neutron scattering (MSANS) instrument [3-6] at guide tube laboratory, Dhruva reactor is discussed along with the illustrations of some recent results.

2. Theoretical Background

The Darwin reflectivity function $R(\theta)$ of a thick perfect crystal near the Bragg angle may be written as

$$R(\theta) = 1;\ |y| \leq 1;\ R(\theta) = 1-(1-y^{-2})^{1/2};\ |y| > 1 \qquad (1)$$

where $y = (\theta - \theta_B)/\Delta\theta_D$ is the dimensionless reduced-angular parameter related to dynamical diffraction, θ is the angle of incidence, θ_B is the related Bragg angle and $\Delta\theta_D$ is the half width of the plateau of the Darwin reflectivity function $R(\theta)$, $\Delta\theta_D$ is given by

$$\Delta\theta_D = \frac{b_c \exp(-W)|F| n\lambda^2}{\pi \sin(2\theta_B)} \qquad (2)$$

where b_c is the atomic coherent scattering length, exp(-W) is the Debye-Waller factor, F is the geometric structure factor for the particular Bragg reflection, *n* is the number of unit cells per unit volume and λ is the wavelength of the neutrons.

In non-dispersive (1,-1) setting of double-crystal based small-angle scattering measurements, the final emergent beam from the analyser crystal lies almost parallel to the incident beam. The angular dispersion of the beam, both for recording and representing rocking curves without and with the sample, is defined by the scattering angle, denoted henceforth by θ. The theoretical rocking curve $I_o(\theta)$ of a double-crystal based instrument is given by the convolution of the reflectivity functions of the monochromator and the analyser crystals. In double-crystal based small-angle scattering, the smearing effects along the horizontal direction is negligibly small in comparison to that along the vertical direction. When both the monochromator and analyser crystals have the same relevant characteristics, then the theoretical rocking curve $I_o(\theta)$ is given by,

$$I_o(\theta) = \int R(\theta')R(\theta' + \theta)d\theta' \qquad (3)$$

The measured rocking curve $I_m(\theta)$ of the instrument is related by the theoretical rocking curve $I_o(\theta)$ by the following relation

$$I_m(\theta) = \int W_v(\theta')I_o(\sqrt{\theta'^2 + \theta^2})d\theta' + B' \qquad (4)$$

where B' is the background arising due to the scattering from air, slits and other possible sources including incoherent scattering from the crystals and $W_v(\theta)$ is the normalized resolution function of the instrument in the vertical direction.

In the Taylor series expansion of $I_o(\sqrt{\theta'^2+\theta^2})$ about θ' = 0, if only the first term $I_o(\theta)$ is retained, then the measured rocking curve $I_m(\theta)$ and the theoretical rocking curve $I_o(\theta)$ become one and the same. Mathematically, this is justified when $I_o(\theta)$ is so sharply falling, vis-a-vis $W_v(\theta)$, that the approximation $I_o(\sqrt{\theta'^2+\theta^2}) \approx I_o(\theta)$, holds good. In the double- crystal based SANS, when multiple bounce channel cut crystals are used as monochromator and analyser, $I_o(\theta)$ becomes very sharply [2] falling and it is possible to measure it directly.

In small-angle scattering, the scattering profiles are expressed in terms of the modulus of wave-vector transfer *q*. In double-crystal based small-angle scattering measurements, the involved scattering angle θ is very small and the relation *q (or Q)* = $k\theta$, where $k(= 2\pi/\lambda)$ is the wave number of the radiation, holds good. The measured scattering profile $I_M(q)$ of a specimen consists of a transmitted part $I_t(q)$, proportional to $I_o(q)$, and the scattering part $I_s(q)$,

$$I_M(q) = I_t(q) + I_s(q) + B \qquad (5)$$

where B is the background arising due to scattering from air, slits and other possible sources including incoherent scattering from the sample, and crystals. If the smearing effect of a measurement on scattering profile is neglected, then the above equation can be rewritten as

$$I_M(q) = \exp(-t\Sigma_{tot})\, I_m(q)\left\{1 + t\Omega \frac{d\Sigma_s}{d\Omega}(q)\right\} + B \qquad (6)$$

where *t* is the specimen thickness; $d\Sigma_s/d\Omega$ (q) is the slit smeared differential scattering cross section of the specimen per unit volume per unit solid angle; Ω is the solid angle involved in the measurement; Σ_{tot} is the linear attenuation coefficient of the system accounting for absorption, incoherent and coherent scattering including small-angle scattering from the specimen. It is interesting to note that since the measurements of both $I_M(q)$ and $I_m(q)$ involves the same detector, the knowledge of detector efficiency is not essential for estimation of $d\Sigma_s/d\Omega$ (q). At zero angle, the double-crystal analyser passes the full intensity of the straight-through beam, hence the measured transmission T_M is given by

$$T_M = \frac{I_M(0)}{I_m(0)} \qquad (7)$$

with the true transmission T_{true} is given by

$$T_{true} = \exp(-t\Sigma_{tot}) \qquad (8)$$

Due to finite non-zero contributions of $d\Sigma_s/d\Omega$ (q) and B at *q* = 0, the measured transmission is always more than its true value. $d\Sigma_s/d\Omega$ (q) is given by the following relation

$$\frac{d\Sigma_s}{d\Omega}(q) = \frac{\left(\frac{I_M(q)-B}{T_{true}} - I_m(q)\right)}{I_m(0)\Delta\theta_h\Delta\theta_v t} \approx \frac{\left(\frac{I_M(q)-B}{T_M} - I_m(q)\right)}{I_m(0)\Delta\theta_h\Delta\theta_v t} = \frac{I(q)}{I_m(0)\Delta\theta_h\Delta\theta_v t} \qquad (9)$$

where $\Delta\theta_h\Delta\theta_v$ defines the pertinent solid angle Ω involved in the measurement and I(q) is the transmission and background corrected recorded scattering profile.

In double-crystal based SANS instrument, the angle in the scanning direction is highly collimated by the crystal optics. Full width at the half maximum (FWHM) of the blank measurement is taken to be $\Delta\theta_h$. $\Delta\theta_v$ is calculated from the ratio of detector aperture to sample-detector distance. When the smearing effect on scattering profile due to instrumental resolution is not neglected, then the expression of $I_M(q)$ can be rewritten as

$$I_M(q) = \exp(-t\Sigma_{tot})\left\{I_m(q) + \iint dq_h dq_v I_0(q_h) W_v(q_v) t \frac{d\Sigma}{d\Omega}\left(\sqrt{(q-q_h)^2 + q_v^2}\right)\right\} + B \qquad (10)$$

where, q_h and q_v are the components of the q in the horizontal and vertical directions, respectively; $d\Sigma_s/d\Omega(q)$ is the desmeared differential scattering cross section of the specimen per unit volume per unit solid angle; $W_v(q)$ is the normalized resolution function of the instrument along the vertical direction in q-space.

Since, generally $I_o(q)$ is a sharply falling, vis-à-vis $W_v(q)$, function of q, to get an initial estimated of $W_v(q)$, the approximation $I_o(q) \approx \delta(q)$ is justified and $I_M(q)$ can be approximated to

$$I_M(q) \approx \exp(-t\Sigma_{tot})\left\{I_m(q) + C' \int dq_v W_v(q_v) t \frac{d\Sigma}{d\Omega}\left(\sqrt{q^2 + q_v^2}\right)\right\} + B \qquad (11)$$

where C' is only a scale factor independent of q. So the transmission and background corrected scattering profile I(q) of the specimen is given by

$$I(q) = C \int W_v(q_v) t \frac{d\Sigma}{d\Omega}\left(\sqrt{q^2 + q_v^2}\right) \qquad (12)$$

where, C is only a scale factor independent of q.

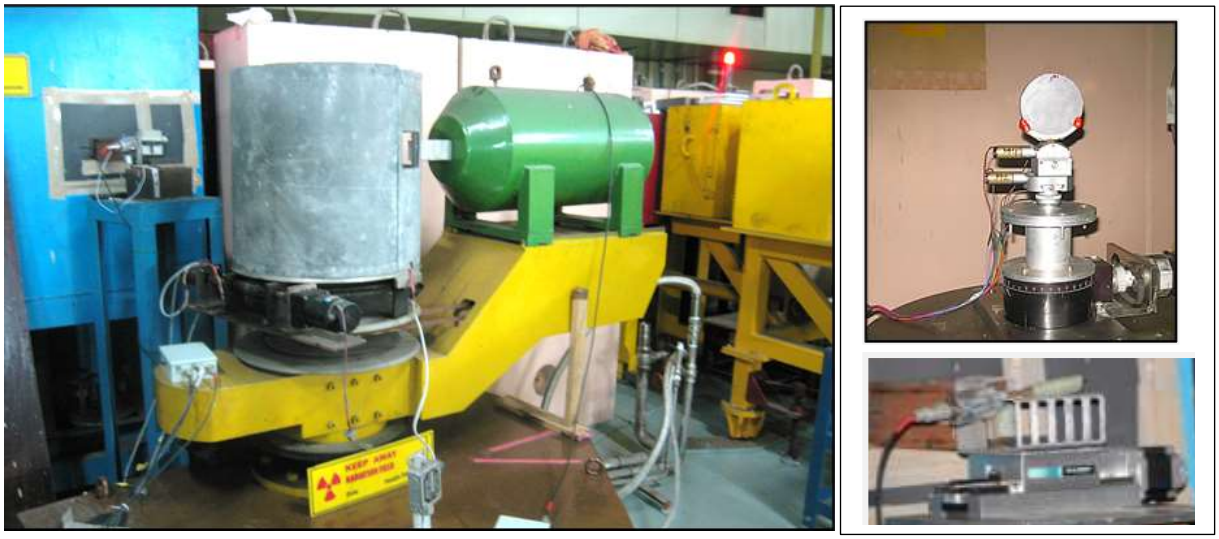

Fig. 1. Double crystal-based MSANS facility at guide tube laboratory, Dhruva. Right panel shows the micro-rotational stage and sample translation stage

3. Instrumental Parameters of MSANS

The photograph of the MSANS instrument at guide tube laboratory, Dhruva reactor is shown in the Fig. 1. Schematic layout of the instrument is illustrated in Fig. 2. The size of the neutron beam coming from the guide is 2.5 cm (horizontal) × 10.4 cm (vertical). Two silicon crystals (diameter 8.25 cm and thickness 0.6 cm) cut parallel to (111) planes are used as monochromator and analyzer. The monochromator crystal reflects neutrons with wavelength $\lambda \sim 0.312$ nm. and $\Delta\lambda/\lambda \approx 1\%$. It is pertinent to note that in the present neutron guide, the horizontal angular divergence of neutron beam of wavelength $\lambda = 0.312$ nm is 0.312°. The monochromator crystal is set on a normal goniometer. The monochromatic neutrons then pass through a one-meter-long cadmium collimator, 2 cm × 5 cm, placed 20 cm away from the monochromator center. In most of the measurements, either circular beam cross section of 1.5 cm diameter is used or rectangular beam

~1.5 cm x 2.5 cm is used. However, depending upon the specimen size, provision has been made to vary beam cross section. The distance between the monochromator center and the sample mount center is 128 cm. The analyzer crystal, placed 100.5 cm away from the sample, is set on a precise goniometer with smallest control step size of 0.0008°. The (111) symmetric reflections are used for both the crystal. Analysed neutrons are detected by a BF_3 proportional counter of 3.81 cm diameter placed 55 cm away from the center of the analyzer crystal. Table-1 provides some relevant parameters of MSANS.

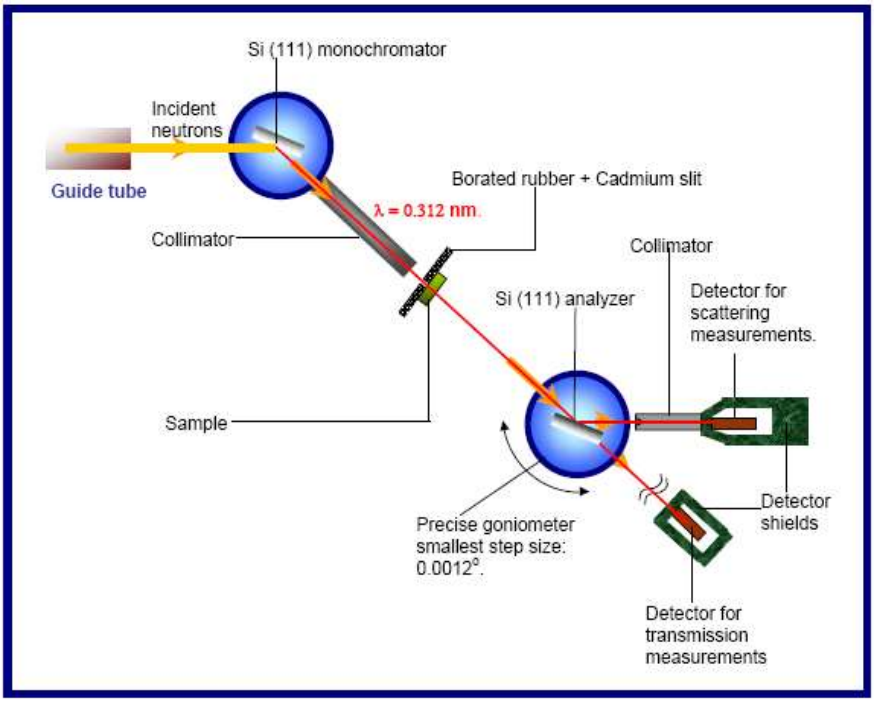

Fig. 2. Schematic layout of MSANS facility

Table 1. Some relevant parameters of the MSANS facility

Beam port	Guide G1
Monochromator	Si(111)
Wavelength	3.12 Å
($\Delta\lambda/\lambda$)	~1 %
Flux at sample	500 n/ cm^2/sec
Analyser	Si(111)
Q range	0.0003 -0.0173 $Å^{-1}$
Real space resolution	200 - 10000 Å
Detector	BF_3
Sample environment	Multi-sample stage (Up to maximum 5 samples) Heating stage (RT to 100°C)

The data acquisition and motor movements are controlled through python-based program (Fig. 3).

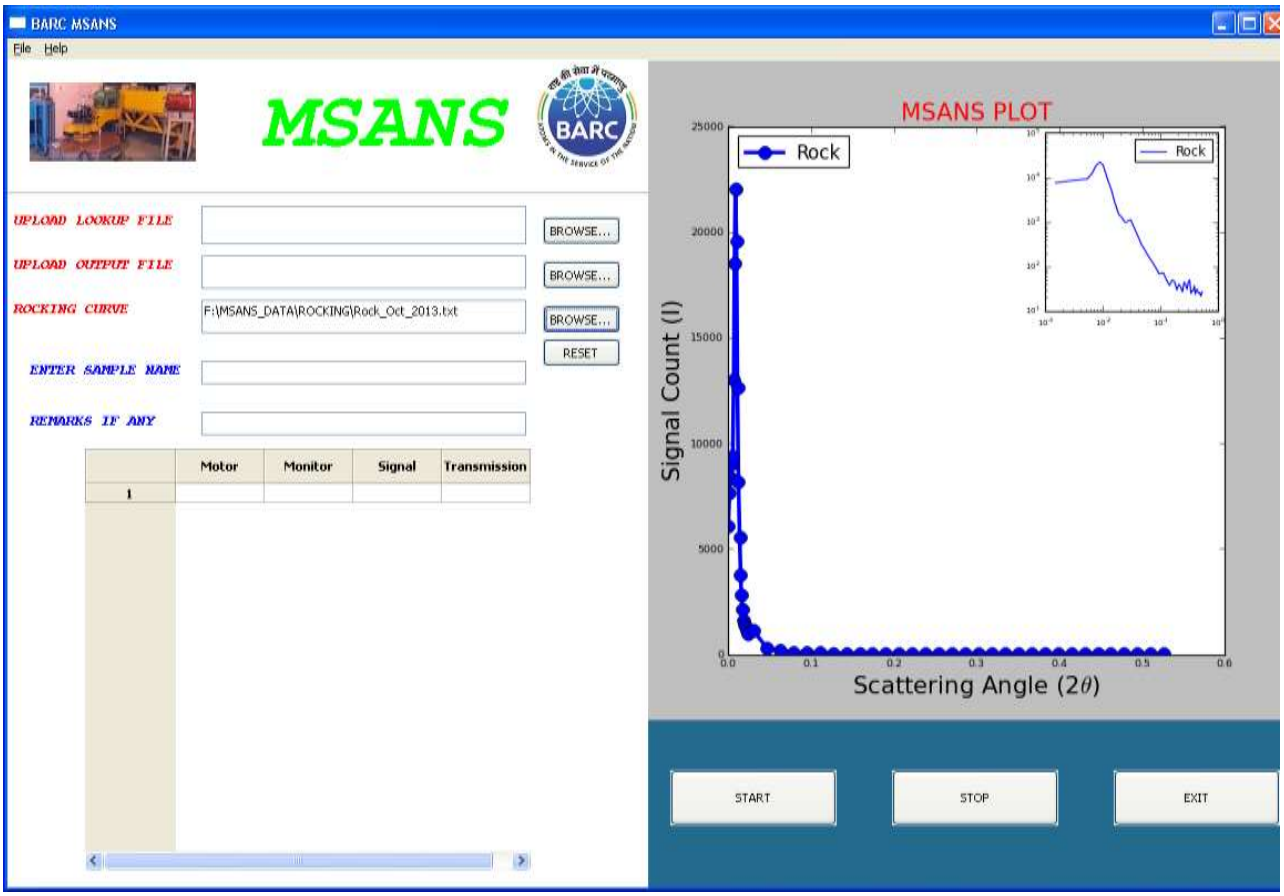

Fig. 3. The python GUI based data acquisition software window for MSANS.

4. A Few Recent Results

MSANS facility has been widely utilized to quantify mesoscopic structural information from a variety of samples, including naturally occurring and synthetic porous materials, self-assembled nanostructured microgranules, metallurgical alloys. Some of the recent examples have been discussed in brief to give a flavour of the capabilities of the facility.

4.1. Hierarchical structure in dendritic fibrous silica nanospheres

Templated nanomaterials play a crucial role in addressing technological challenges in several domains including energy, environment and health. Microemulsion-templated dendritic fibrous nanosilica (DFNS) has attracted considerable attention owing to their unique accessible pore structure and high-surface-area but their complex structural hierarchy is still intriguing. Evaporation induced assembly of such nano-silica with amine-based polymers has shown tremendous potential for CO_2 capture. DFNS has shown immense potential for various applications primarily owing to its facile synthesis process, easily accessible surface area and up scalability but its complex structural hierarchy is still intriguing. The formation mechanism of such hierarchical pore morphology in these nanospheres is elucidated and it is observed that a relative variation in periodicity, sheet thickness, and their correlation significantly affects the specific surface area and pore structure, which is strongly influenced by hydrolysis rate and reaction time. Using MSANS data [7] (Fig. 4), a new length scale of the pores is discovered which was otherwise not visible by any other conventional technique.

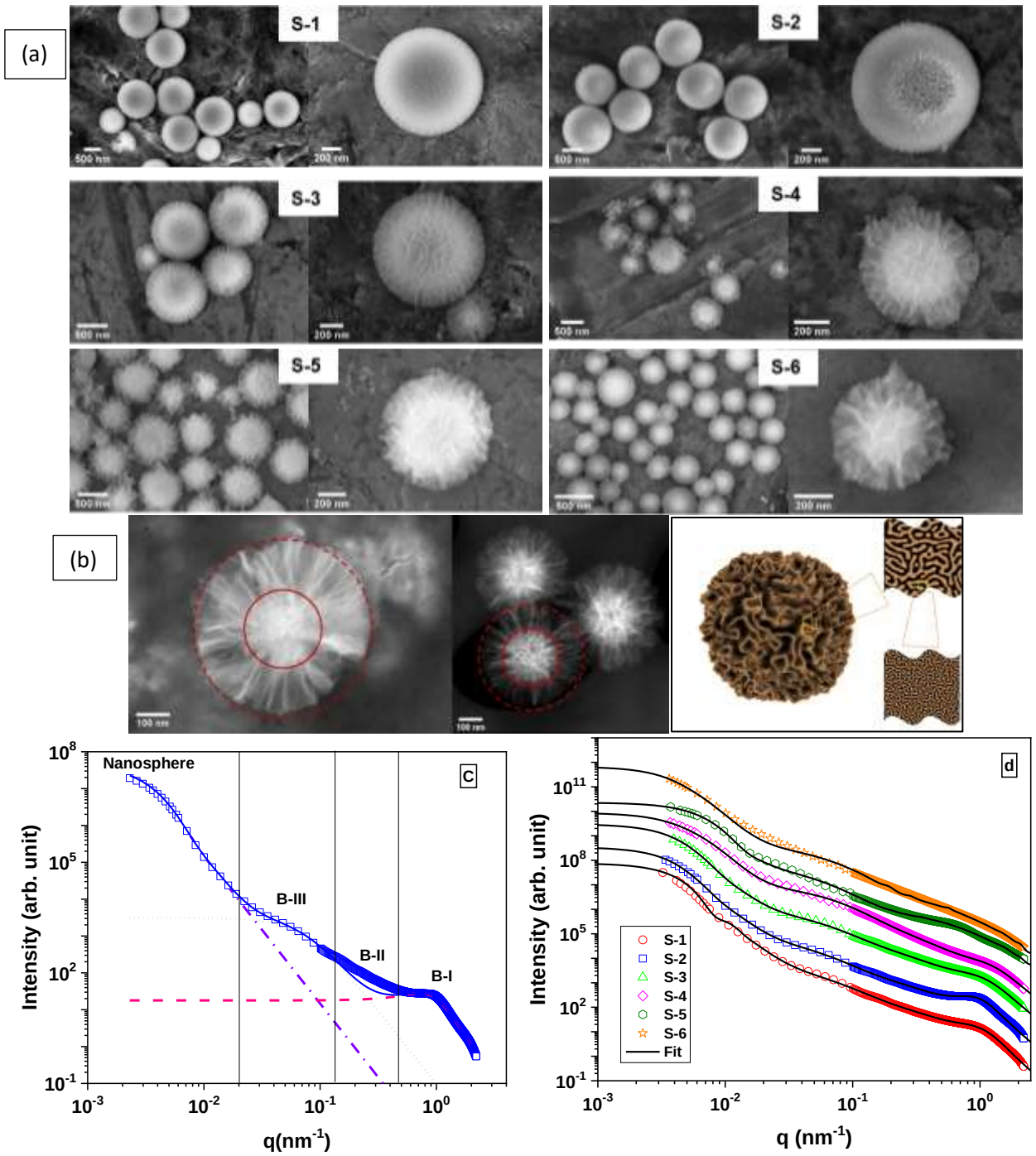

Fig. 4. (a) Micrographs of the dendritic fibrous silica nanospheres varying texture obtained at different synthesis conditions (b) Multi-level structure is discernible in the micrographs with proposed structure model (c) The Teubner-Strey model (continuous blue curve) of nanospheres with two-levels (k=2) of bicontinuous structure is compared with the experimental data (S-2). It is evident that the model deviates at around q~0.4 nm^{-1} and consideration of three levels (k=3) of bicontinuous contributions was found indispensable to explain the data over the entire accessed q range. (d) Fit of the above model to the combined SANS/SAXS data considering three bicontinuous contributions (k=3) for the internal structure of the nanospheres. It is seen that the model can explain well the scattering data of each sample spanning nearly three decades of q. Data sets in (a) and (d) are shifted vertically for clarity.

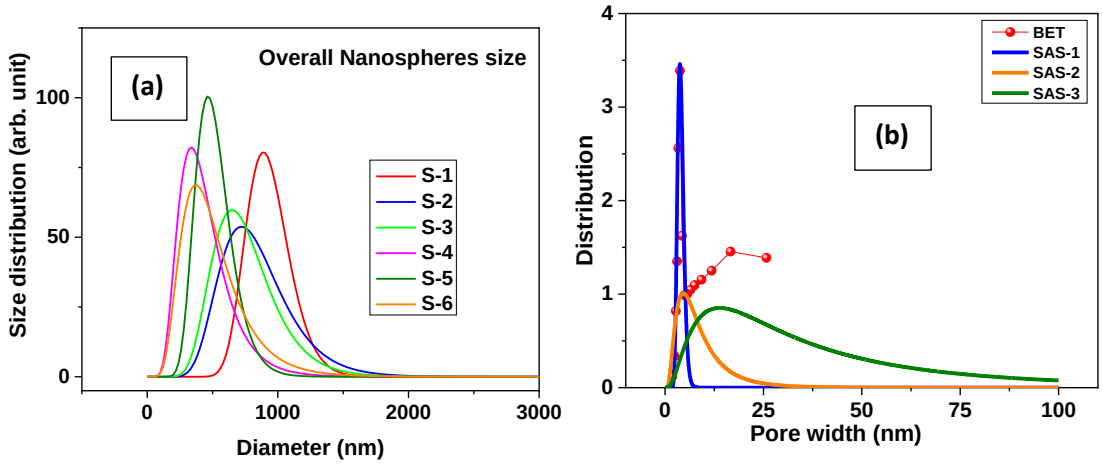

Fig. 5. (a) Size distribution of the nanospheres from the scattering analysis. (b) Comparison of BJH pore size distribution for sample S-1 with pore size distribution obtained from small-angle scattering. SAS-1,2 and 3 are the distributions for the pore width obtained from three bi-continuous contributions.

In case of DFNS, the total scattering intensity will have additive contribution ($I_{int}(q)$) that arises from the scattering by the internal structures and the overall of nanoparticles, thus the resulting intensity can be written as,

$$I(q) \cong I_{sph}(q) + I_{int}(q) \qquad (13)$$

where

$$\boldsymbol{I_{sph}(q) = n(\Delta\rho)^2 \int_0^\infty P(q,R) V^2(R) D_{sph}(R) dR} \qquad (14)$$

where $P(q,R)$ represents the form-factor of a spherical particle having radius R

$$P(q,R) = 9\left(\frac{\sin(qR) - qR\cos(qR)}{(qR)^3}\right)^2 \qquad (15)$$

$V(R)$ is the volume of the particle, n is the number density, $(\Delta\rho)^2$ is the scattering contrast. D_{sph} was considered as lognormal distribution.

According to Teubner-Strey model, the scattering from the bi-continuous microemulsion is given by

$$I_{bm}(q) = \frac{C_0}{a_2 + c_1 q^2 + c_2 q^4} \qquad (16)$$

with $a_2 = \left(1 + \left(\frac{2\pi\xi}{d}\right)^2\right)^2$ $c_1 = 2\xi^2\left(1 - \left(\frac{2\pi\xi}{d}\right)^2\right)$ and $C_2 = \xi^4$ where d represents the periodicity and ξ is the correlation length. 'C_0' is the scale factor and is given by $8\pi\phi(1-\phi)(\Delta\rho)^2 c_2/\xi = 8\pi\phi(1-\phi)(\Delta\rho)^2\xi^3$. Thus, ξ represents the typical thickness of bi-continuous sheet, 'd' is the centre-to-centre distance between the two sheets and ϕ represents the volume fraction of the sheets. While fitting, it was realized that consideration of a polydispersity in 'd' was necessary. A lognormal distribution, $D(d)$ with median d_0 and polydispersity index σ was considered.

$$D_{bm}(d) = \frac{1}{\sqrt{2\pi d^2\sigma^2}} \exp\left[-\frac{(\ln(d/d_0))^2}{2\sigma^2}\right] \qquad (17)$$

If the bi-continuous structure exist over hierarchical length scale then the total intensity in the wide accessible q range can be expressed as

$$\boldsymbol{I(q) = I_{sph}(q) + \sum_0^k I^k{}_{bm}(q)} \qquad (18)$$

where $\boldsymbol{I^k{}_{bm}(q)}$ represents the contribution from k^{th} bi-continuous structure within DFNS. The estimated size distribution of the overall DFNS spheres and the nanopores are shown in Figs. 5a and 5b, respectively.

4.2. SANS predicts the mechanism of shale formation

Shale gas exploitation in the United States has changed the energy dependency on imports and inspired exploration in Canada, China, Australia, and other countries. In an Indian context, potential for shale gas development exists in the Cambay basin in western India, the Krishna-Godavari basin along the east coast of India, the Cauvery basin in southern India, and the Damodar valley basin in eastern part of India. The Indian shales with varying mineral compositions and organic contents has been investigated in detail by ultra-small-angle neutron scattering and small-angle X-ray scattering. The variation of depth dependence fractal dimension of shales as revealed by SANS shows[8-11] strong dependence on pore smoothening by the transport of the fluid over the long period of time which is corroborated by the Monte-Carlo based simulations. Further, the origin of high surface fractal dimension in shale observed by SANS is explained by the simultaneous deposition and dissolution under digenetic conditions. A vast amount of data related to pore morphology and porosity is generated using SANS which will be helpful to predict the shale gas storage capacity in Indian shale. The MSANS-SAXS data from the shale rocks obtained at different depth is fitted using two approaches as outlined below:

It is evident from Figure 6 that SAXS profiles depict power law behaviour with at low-q due to fractal nature of the shale. The low-q deviation is attributed to the fractal upper cut-off, ξ where fractal nature of the surface breaks down.

Surface fractal model with an upper cut-off has been previously used for analysis of the shale samples.

$$I(q) = A.q^{-1}\Gamma(5 - D_s)\xi^{5-D_s}[1 + (\mathrm{q}\xi)^2]^{(D_s-5)/2}\sin[(D_s - 5)\ tan^{-1}(\mathrm{q}\xi)] + B \qquad (19)$$

where A is a q-independent constant and is related to the surface area of the pore-matrix interface and the scattering contrast between pore and its surrounding matrix. D_s is the surface fractal dimension and it varies between 3 to 4. For a smooth surface Ds is close to 2 and for an extremely rough surface it is nearly equals to 3.

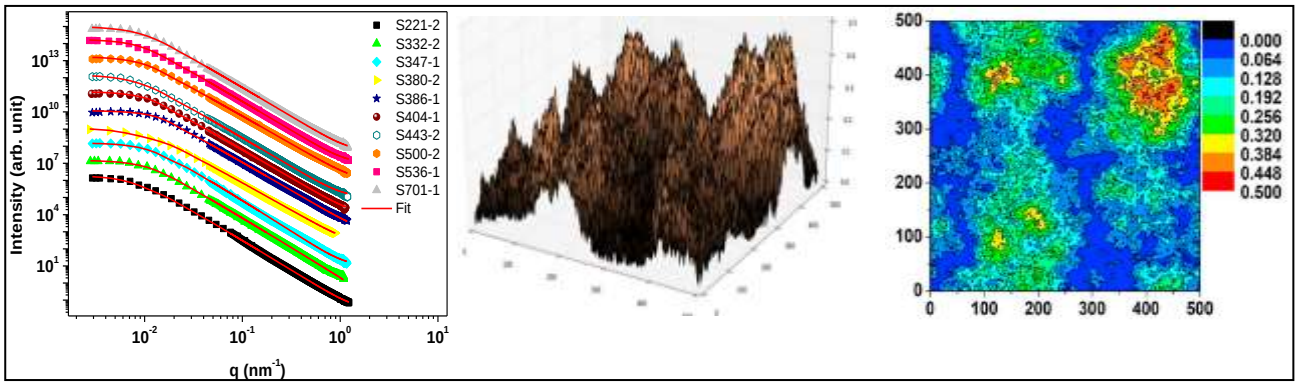

Fig. 6. Combined SANS/SAXS data spanning over nearly three decades in q. The simulated fractal surface mimicking shale surface.

Further in another approach, it is assumed that independent randomly oriented scatters of any shape having power law pore size distribution, f(r) gives rise to the power law scattering in small-angle regime. The polydisperse spherical pore (PDSP) model can be used to describe several aspects of the morphology of sedimentary rocks as well.
The information of pore size distributions in the shale rocks are quite important as far as its practical usage in predicting gas producing capabilities in concerned.

The scattering profiles have been fitted using the expression shown below:

$$I(q) = \sum_i C_i \int_{R_{mini}}^{R_{maxi}} r^6 F(q,r) f(r, D, R_{mini}, R_{maxi}) dr \qquad (20)$$

where C_i is q independent constant and $f(r, D, R_{min}, R_{max})$ is the power law pore size distribution.

$$f(r, D, R_{min}, R_{max}) = \frac{\left[r^{-(1+D)}\right]}{\left[\frac{R_{min}{}^{-D} - R_{max}{}^{-D}}{D}\right]} \qquad (21)$$

and F(q,r) is form factor corresponding the spherical pores of radius r

$$F(q,r) = \left[\frac{3\sin(qr) - qr\cos(qr)}{(qr)^3}\right]^2 \qquad (22)$$

For a surface fractal system, the power law exponent D becomes equal to surface fractal dimension D_s. The fitting of the scattering profiles using power law pore size distribution (eq. 21) is shown in Fig. 6. The fitting of the experimental profiles using the model described above is quite good.

A comparison between the total pore volume calculated using N_2-DFT and the SANS study is used to highlight the difference between accessible and total pore volume. It is found that the surface fractal dimension of accessible pores is lower than that of inaccessible pores in the shale studied, suggesting that the pore interfaces of accessible pores are smoother. This smoothness is likely due to fluid invasion-induced weathering, a diffusion-controlled process. Since nanoporous shale rocks are characterized by low porosity and permeability, the weathering process in such systems remains slow and diffusion-limited. It is well-established that mineral-fluid interfaces regulate dissolution rates in rock systems. Previous models, such as Monte Carlo simulations, have been applied to predict fractal dimensions and surface roughness in sedimentary rocks undergoing diagenesis. However, the smoothening of accessible pore surfaces in rocks is yet to be thoroughly explored.

In this study, we model the diffusion-controlled smoothening of the accessible pore interface using a Monte Carlo simulation. The model simulates matter transport from areas of high to low curvature within the pore-matrix interface, a method previously applied to explain surface smoothening during sintering processes. The simulation generates an initial self-affined fractal surface, which undergoes a gradual smoothening with increasing Monte Carlo (MC) steps. Figure 6 illustrates the generated surface with an initial fractal dimension of 2.7. Additionally, we studied the effect of the β factor—related to particle binding in the pore matrix—on the evolution of the surface fractal dimension . Higher β values led to more rapid smoothening, while lower β values caused slower changes. Given that shale pore matrices are composed of various minerals (quartz, clay, carbonates, and organic matter), the β factor, and thus the rate of smoothening, depends on the constituent material.

Our simulation results align with experimental observations from SAXS/SANS data, which show that the fractal dimensions of inaccessible and accessible pores are approximately 2.7 and 2.5, respectively, for most shales. This suggests that the smoothening of accessible pores leads to a lower

surface fractal dimension. Our findings demonstrate that while the deposition and dissolution processes during shale formation under diagenetic conditions initially dictate pore roughness, the subsequent smoothening in accessible pores is driven by pore fluid invasion. Elevated geological temperatures may further influence this mass transport process, although it is expected to affect both accessible and inaccessible pores uniformly.

4.3. Hierarchically structured nanostructured micro-granules

Within the material science and engineering communities, there has been a long-standing interest in understanding the behavior of granular materials, which are defined as conglomerates of discrete solid particles[12]. These materials exhibit properties that are markedly different from those of conventional solids, liquids, or gases, prompting their classification as a distinct form of matter. More recently, granular materials have also been recognized by physicists as a model system for studying driven dissipative systems far from equilibrium. Beyond their scientific significance due to complex structural and flow properties, granular materials are integral to numerous industries, including mining, agriculture, civil engineering, and pharmaceuticals. In everyday life, granular materials typically appear at the macroscopic scale, such as clay, powder, sand, and foams. However, in the past few decades, growing attention has focused on synthesizing granular materials with smaller dimensions, in the micrometric or sub-micrometric range. Such hierarchical structuring provides these micro-granules with unique properties, including enhanced surface area, controlled porosity, and tunable mechanical or chemical attributes[13-15]. These features make them ideal for applications in fields like drug delivery[16, 17], catalysis[18, 19], energy storage[20, 21], and environmental remediation[22, 23]. For example, in drug delivery, the nanostructured surfaces can improve loading capacity and enable targeted release, while in catalysis, they can enhance reaction kinetics by increasing active surface sites. Hierarchically decorated nanostructured micro-granules thus represent a sophisticated class of materials engineered for advanced functional applications.

Advanced synthesis methods, including both top-down and bottom-up approaches, have been developed to fabricate these materials with tailored properties. When composed of nanoparticles, these granular materials exhibit unique physical and chemical attributes, such as high specific surface areas and quantum confinement effects[24-26]. Additionally, nanostructured granular materials are inherently micro- to mesoporous, with nanoscale interstitial spaces that facilitate fluid transport and enable novel phenomena[13-15, 22]. Among several strategies employed to create such nanostructured granular materials, evaporation-induced self-assembly (EISA) via **spray-drying** has been a technique widely utilized, particularly in food and pharmaceutical industries[27-30]. Spray-drying involves drying atomized liquid colloid laden droplets into powder form and over the years it has been adapted to nanoscience and technology, enabling the fabrication of nanostructured micro-granules. This one-step facile process results in formation of hierarchically decorated nanostructured micro-granules as depicted in Fig. 7a. During drying of the colloidal droplet, the cohesive capillary force provides the necessary external drive to overcome this potential hill, and subsequently, the colloidal nanoparticles get interlocked in form of an assembled granular structure. EISA in a contact-free droplet results in the formation of a micro-particle of well-defined shape comprised of correlated nanoparticles unlike the case of diffusion-limited aggregation where fractal-like agglomeration takes place owing to uncontrolled agglomeration of the nanoparticles. As the spray-dried nanostructured granular materials exhibit hierarchical structures, ranging from nanometric building blocks (a few nanometers) to assembled microscopic structures (a few microns)[31], small-angle scattering (SAS)[32, 33] is a powerful, non-destructive technique that probes density fluctuations across these length scales. The systematic characterization by SAS provides

reciprocal space data that can be analyzed to extract morphological information, such as particle size, shape, size distribution, and positional correlations[33, 34]. Fig. 7b shows a typical SAS profile of spray-dried micro-granules comprised of nearly monodisperse silica nanoparticles. The scattering profile reveals multi-length scale hierarchical structures. The scattering signal at higher Q-range is primarily dominated by the structure and interaction of individual building blocks, while scattering intensity at lower Q-range originates from the large-scale structural assembly of individual building blocks. In the following part of this article, we discuss a few illustrative scientific results based on such hierarchically decorated nanostructured micro-granules.

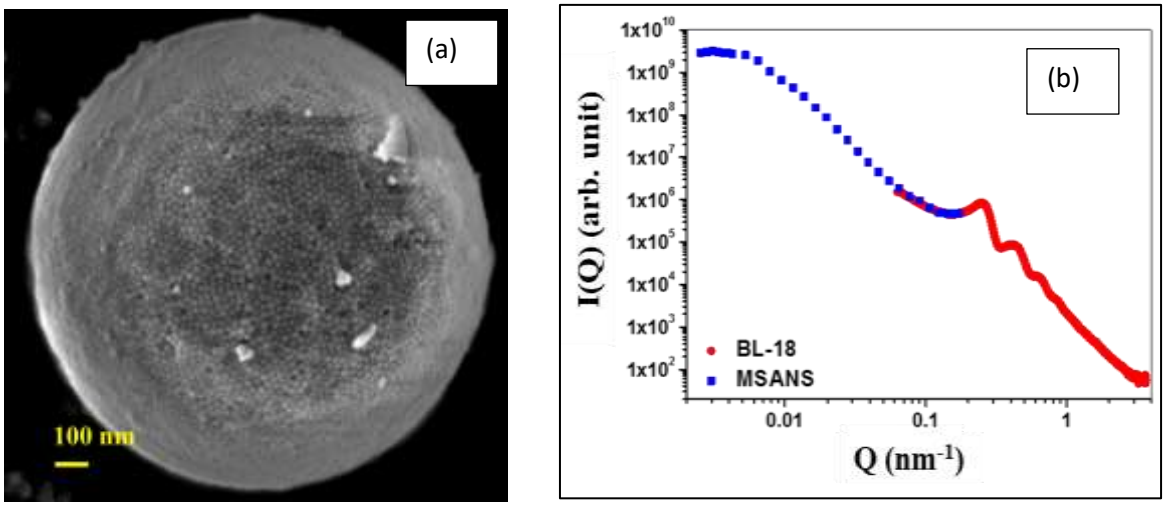

Fig. 7. (a) Electron micro-graph of a spray-dried micro-granule decorated with highly correlated silica nanoparticles. (b) The scattering profile of the silica micro-granule reveals hierarchical multi-level structure. MSANS profile in 'blue' overall granule and clusters made of silica whereas SAXS profile collected at BL-18 reveals the positional correlation of the individual silica nanoparticles as building blocks.

4.4. Temperature mediated morphological transition of micro-granules

Understanding the transformation of a dilute evaporative colloidal spray droplet into a micro-granule with distinct morphology holds significant scientific and technological importance. This study demonstrates that the morphology and size distribution of microcapsules can be precisely controlled by altering the drying temperature. The shapes and sizes of the capsules were systematically analyzed at four different drying temperatures, revealing a gradual transition in morphology from spherical to toroidal as the temperature increased from 110°C to 180°C, as shown in Fig. 8[35, 36]. A plausible mechanism detailing the chronological pathway of this morphological transformation is proposed as follows. At lower temperatures, nanoparticles assemble densely, forming spherical granules with a narrowed size distribution compared to the original droplets. As the drying temperature increases, larger hollow capsules are formed, characterized by nanoparticles arranged into thinner shells due to their preferential motion under the temperature gradient. At even higher temperatures, the shell undergoes buckling, resulting in toroidal granules, accompanied by increased polydispersity in granular size. The experimentally observed transitions are supported by computer simulations, while the variations in hollowness and the propensity for buckling of the capsules are thoroughly analyzed using scattering and imaging techniques. The observed shape evolution aligns with Surface Evolver computer modeling[37], which incorporates the buckling of elastic shells influenced by drying rates. Fig. 9(a) depicts the scattering profiles of micro-granules synthesized at different temperatures. Plausible mathematical model was constructed to

fit the experimental profiles. Despite significant changes in external morphology, the average volume fraction of correlated nanoparticles within the granules remained nearly unchanged throughout temperature variations. The shape transition and the increase in overall granular size at higher drying temperatures can be explained by two possible scenarios: (i) nanoparticles forming a well-packed shell enclosing a hollow core, or (ii) the formation of ramified fractal-like aggregates of nanoparticles within the granules. However, by evaluating the scattering profiles the distinction between these two cases can effectively be determined. The positional correlation among the individual silica nanoparticles does not change which confirms that the larger capsule size and buckling at higher temperatures are attributed to the presence of an internal hollow core rather than non-consolidated fractal-like aggregates, as demonstrated in Fig. 9(b).

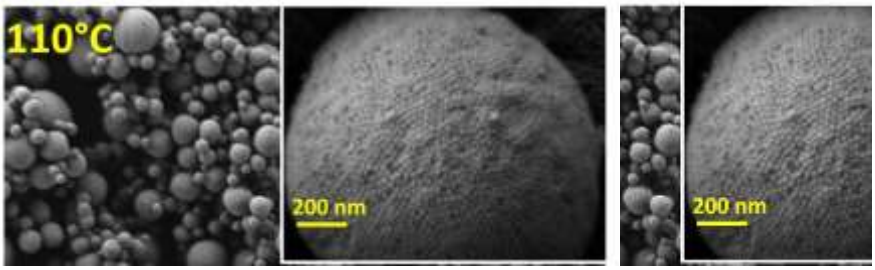

Fig. 8. Electron micrographs reveal morphological transition from sphere (at 110°C) to doughnut shaped (at 180 °C) micro-granules. At 130°C, the micro-graph shows some deformed spherical micro-granules, whereas at 160°C, it shows a mixture of spheres and doughnut shaped micro-granules. Inset to each figure shows the magnified image of the correlated silica nanoparticles.

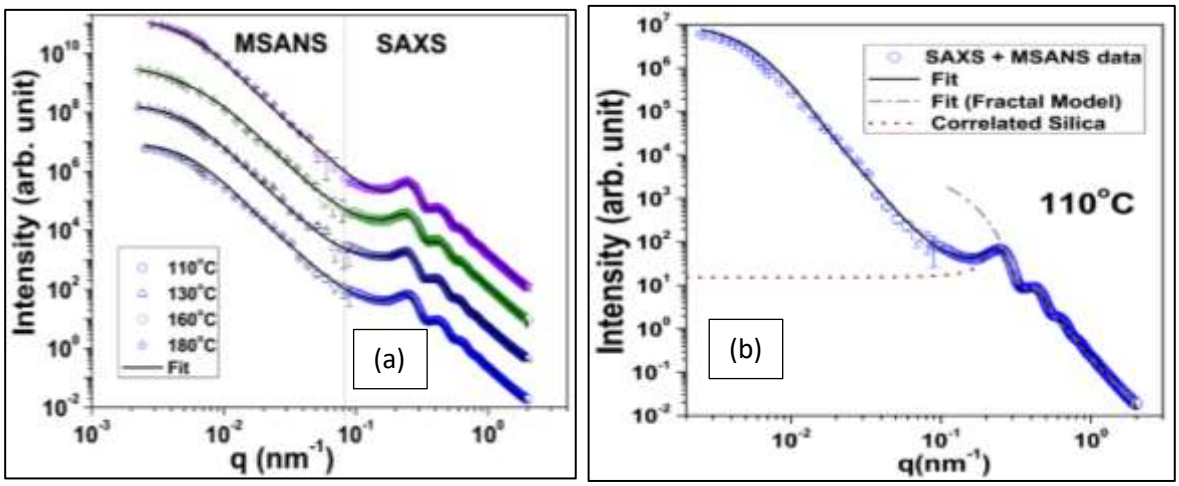

Fig. 9. (a) Intensity profiles over the whole accessible Q-range. The profiles are vertically shifted for better clarity. (b) Depicts the scattering intensity profile collected on micro-granules synthesized at 110 °C. Solid line represents the mathematical model fitting to the experimental data. The dashed and dotted lines show different fitting models to understand the correlation of inter-locked silica nanoparticles within the micro-granule. The fractal like correlation does not exist among the randomly jammed silica nanoparticles.

4.5. Nano-confinement induced nucleation and growth in porous matrix

Another example of the unique feature of trapped water in interstitial mesopores of micro-granules is demonstrated in the following research. This research explores the role of nanoscale confinement in the formation and growth of silver nanoparticles within porous silica micro-granules synthesized through a spray-drying process[14]. Colloidal silica nanoparticles along with silver nitrate salt, as a

precursor of silver nanoparticle, were spray-dried to synthesize composite micro-granules. These nanostructured granules provide a confined environment that accelerates the reduction of silver nitrate to metallic silver nanoparticles compared to reactions in bulk solutions. SANS, SAXS, and field emission scanning electron microscopy (FESEM) were employed to analyze the structure and formation mechanisms. The FESEM images revealed the formation of micrometric granules with distinct patches of silver nanoparticles, both isolated and aggregated, on the silica surface, as depicted in Fig. 10(a). The scattering profile was collected over a wide-Q range that reveals the overall granular structure as well as positional correlation of both silica and silver nanoparticles [Fig. 10(b)]. The study found that the interstitial pores in the silica granules, with an average size of 9 nm, play a crucial role in enhancing the reaction kinetics. These pores create spatial confinement, which increases the likelihood of interaction between silver nitrate and silanol groups present on the silica surface. This confinement effect, combined with the retention of bound water molecules in the mesopores, significantly enhances the reduction of silver ions. Under X-ray irradiation, the bound water dissociates to form hydrated electrons, which further accelerate the reduction process and facilitate nanoparticle growth. Time-resolved scattering analysis revealed that the size of silver nanoparticles increased progressively under X-ray exposure, with the structural correlation among silica particles evolving in response to nanoparticle growth.

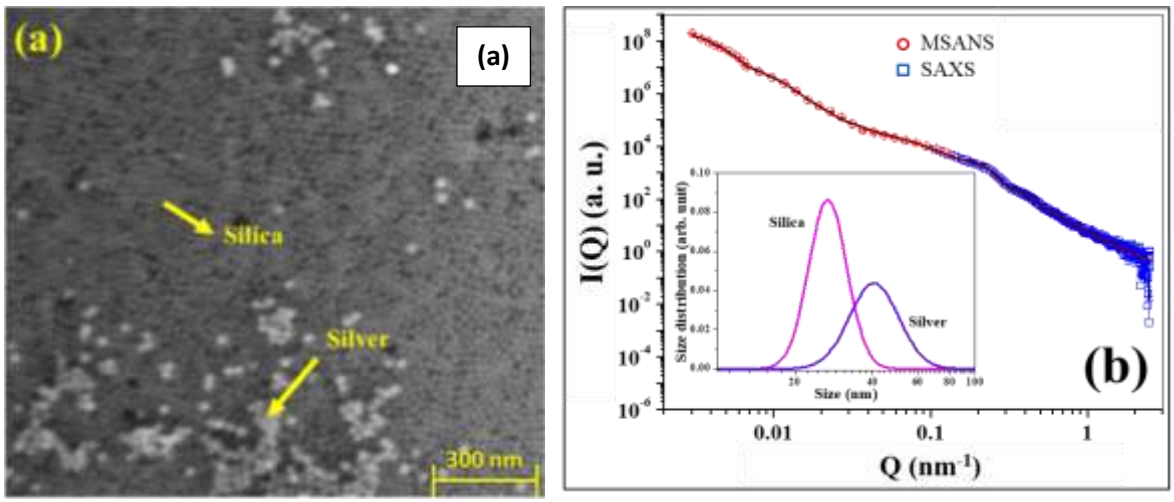

Fig. 10. (a) FESEM image of silica-silver nanocomposite micro-granules. Bright particles are silver nanoparticles grown on the surface of porous silica matrix. (b) Scattering profile of silica and silver nanocomposite micro-granules. The Solid line denotes the mathematical model fitting to the experimental scattering profile. The figure in inset shows the estimated size-distribution of both silica and silver nanoparticles.

4.6. Packing of shape-anisotropic nanoparticles in a microsphere

Let us now demonstrate another aspect of evaporative self-assembly of colloidal nanoparticles with respect to the role of shape anisotropy of the individual building blocks. The arrangement of particles is a common phenomenon and holds significant importance, especially in materials science at the nanoscale. The complexity increases when the particles differ from spherical shapes, making it challenging to measure their positional and rotational correlations. Accurately estimating the packing fraction requires an in-depth analysis of the positional arrangement of densely packed particles. The following example demonstrates an innovative approach for calculating the packing fraction of highly correlated nano-ellipsoids within a microsphere by employing small-angle

scattering. The approach is demonstrated through the analysis of structural correlations among nano-hematite ellipsoids in three-dimensional micrometric granules, created using a rapid evaporative self-assembly process[38, 39]. Fig.11 (a)-(d) shows the electron micrographs of spray-dried micro-granules comprised of hematite nano-ellipsoids of aspect ratio (AR) ~2 and ~4. Strong short-range positional correlation is observed in the micro-granules which suggest a dense packing of randomly jammed nano-ellipsoids. However, conventional methods of analyzing scattering data are inadequate for capturing the actual packing fraction of these anisotropic particles due to their deviation from spherical symmetry. The orientation variations of the packed anisotropic particles de-smear the structural correlations, of the jammed particles deviates from spherical shape, then the relative orientation of the particles plays an important role in the correlated structure. SAS profiles shown in Fig. 12(a) of P-2 (with AR~2) and P-3 (with AR~4) micro-granules do not show any strong positional correlation because of the de-smearing of structure factor owing to the distribution in relative orientations of nano-ellipsoids. When a spherical particle is elongated along one or more directions, the spherical isotropic symmetry is broken and because of the shape-anisotropy of the particle, the relative orientation becomes an additional degree of freedom during the jamming process. This research highlights the necessity of incorporating an inter-particle distance distribution function in the structure factor analysis to accurately determine the packing fraction of correlated nano-ellipsoids. A negatively skewed distribution function, such as the Weibull distribution [Fig.12(b)], enables to effectively model the inter-particle distances among jammed non-spherical particles. This approach yields realistic estimates of the local packing fraction, approximately 0.67 and 0.65 for ellipsoids with AR ~2 and ~4, respectively, within micro-granules.

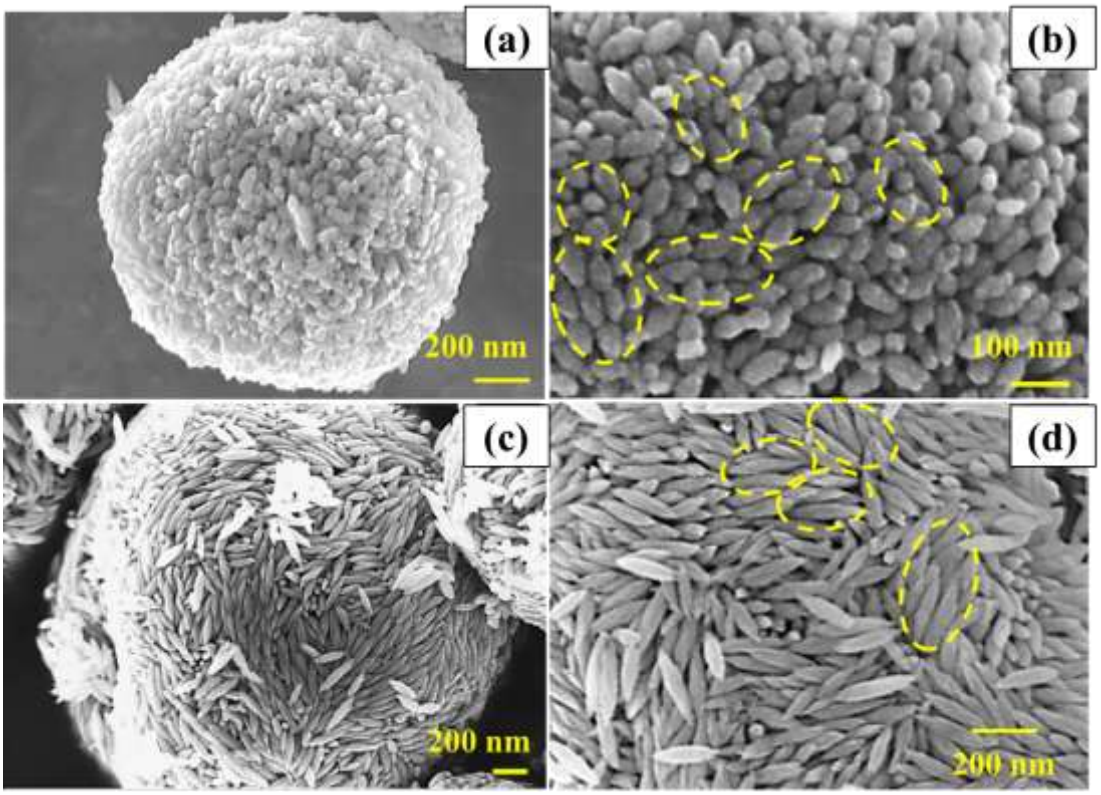

Fig. 11. Electron images of micro-granule comprised of nano-ellipsoids of AR ~2 [(a)& (b)] and AR ~4 [(c) & (d)]. (b) & (d) Shows the magnified image of the surface of micro-granule revealing the correlated nanostructure. The dotted circles shown as a 'guide-to-eye' to the localized packing of the ellipsoids.

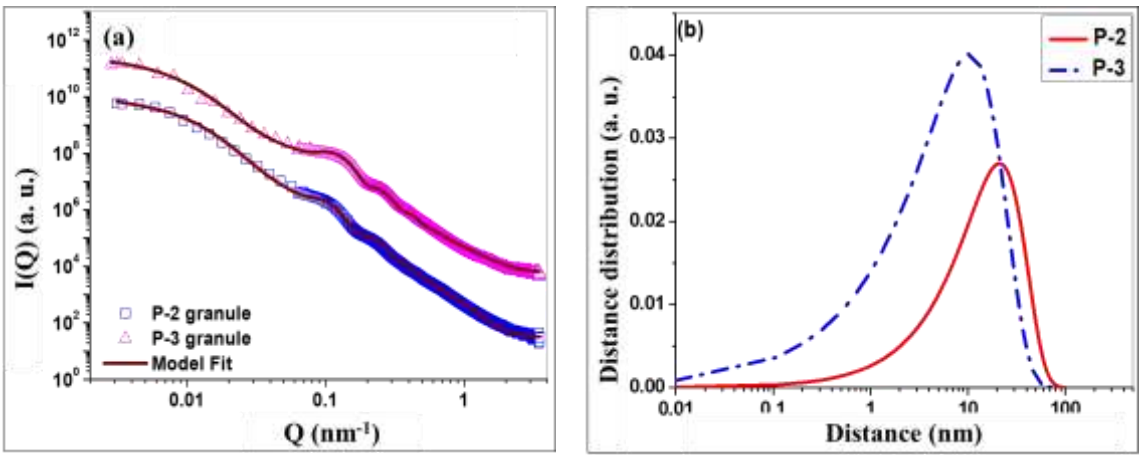

Fig.12. (a) SANS data along with model fitting considering the effective structure factor function using Weibull distance distribution function. (b) The Weibull distribution of the inter-particle separation distance of jammed ellipsoids within the micro-granules.

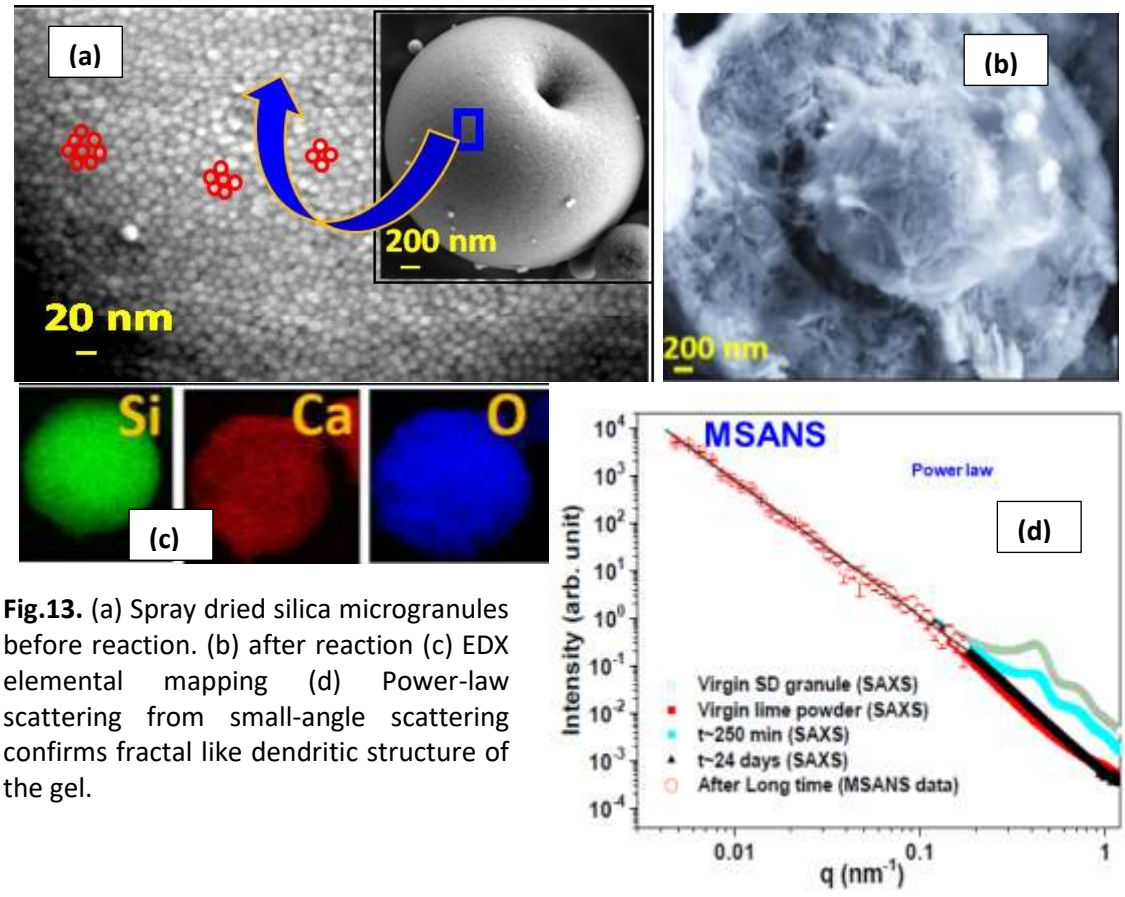

Fig.13. (a) Spray dried silica microgranules before reaction. (b) after reaction (c) EDX elemental mapping (d) Power-law scattering from small-angle scattering confirms fractal like dendritic structure of the gel.

4.7. Pozzolanic gelling in in spray-dried silica microgranules

Continuously increasing greenhouse gas emissions and resulting global worming have directed researchers towards development of alternative processes to reduce environmental impact of construction and building industries. In recent years, there have been lot of efforts to replace cement by introducing pozzolans from waste by-products, such as fly ash, silica etc. Pozzolans are primarily siliceous/aluminous substances, which themselves possess no cementitious value,

however, in presence of moisture, they chemically react with alkali hydroxide to form compounds having cementitious properties. Calcium hydroxide ($Ca(OH)_2$)) and spray dried silica microgranules (Fig. 13(a)) were mixed together well in 70:30 weight proportion. Its structural evolution over time was measured[40] using synchrotron based small-angle X-ray scattering. The power law scattering over a wide q range (Fig. 13(d)))using MSANS data[40] helped[40] to identify the formation of dendritic fractal-like structure (Fig. 13(a)) owing to the pozzolanic gelling as also confirmed by FESEM. Signature of power law behaviour over a wide q range is evident from the Fig 13 (d). Elemental mapping of the reacted granules confirms the uniformity of Si, Ca and O (Fig. 13 (C)).

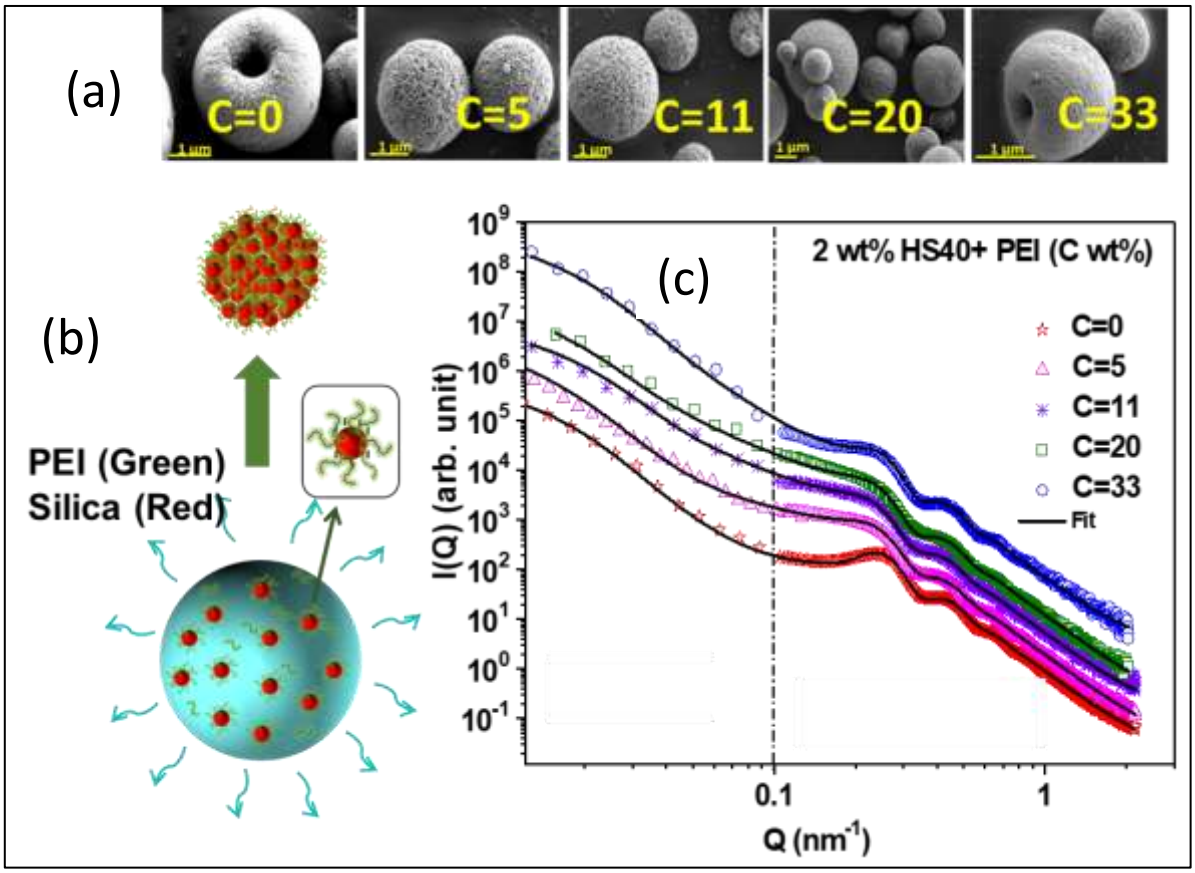

Figure 14. (a) FESEM micrographs of nanostructured microgranules with varying PEI loading. (b) The schematic of cooperative assembly via droplet drying (c) The MSANS data at low-Q with complementary SAXS data at high-Q.

4.8. Hierarchically structured microspheres for CO_2 capture

Anthropogenic CO_2 emissions, largely resulting from the combustion of fossil fuels, industrial activities, and deforestation, are a key contributor to climate change. These emissions elevate atmospheric CO_2 concentrations, intensifying the greenhouse effect, which traps heat in the Earth's atmosphere and drives global warming. CO_2 capture is an essential technology designed to mitigate greenhouse gas emissions by capturing carbon dioxide either from industrial processes or directly from the atmosphere. [41]. Silica-PEI nanoadsorbents represent a promising new class of materials engineered for the efficient capture of carbon dioxide (CO_2), tackling the global challenge of reducing greenhouse gas emissions[42]. These hybrid materials combine the high surface area and porosity of silica nanoparticles with the CO_2-capturing properties of polyethyleneimine (PEI), a

polymer abundant in amine groups that readily reacts with CO_2. This synergy makes silica-PEI nanoadsorbents a highly promising solution for carbon capture and sequestration (CCS) technologies. However, existing methods for producing these nanoadsorbents are complex and face scalability challenges. For the first time, the cooperative assembly of oppositely charged silica colloids and PEI has been employed to create silica-PEI microspheres with tunable loading and porosity[42, 43]. Figure 14a presents a schematic of the assembly process of silica and PEI during droplet drying, while Figure 14b shows the morphology of the microspheres at various PEI loadings obtained from this assembly process. These microspheres exhibit a hierarchical structure that requires a wide Q-range for analysis. The double-crystal MSANS diffractometer at the Dhruva reactor is a unique facility in the country, providing access to low-Q ranges and enabling the probing of hierarchical structures up to a size range of 1000 nm.

Figure 14c presents the MSANS data, showcasing the multi-level structures within the microspheres. The analysis reveals both the nanoparticle packing fraction and the intermediate structures of the microspheres. These tunable microgranules have shown great potential for CO_2 capture, with sorption capacity strongly influenced by nanoparticle jamming, which can be optimized by adjusting various morphological factors.

4.9. Phase separation in high entropy alloy during spark plasma sintering

Recently, multi-component multi-principal element alloys or high entropy alloys have generated interesting scientific curiosity. Many of these single-phase solid solutions are found to undergo fascinating phase transformation; leading to formation of dual or even multiphase microstructure. In the present investigation, a nano-scaled phase separation of equiatomic mechanically alloyed CoCuFeNiTi FCC phase is investigated with detailed microstructural characterization at all length scales. The single-phase FCC alloy is found to first undergoes phase separation to BCC (Ti) solid solution and FCC (Co,Cu,Ni)-rich solid solution, which again separates into two new FCC phases; (Cu,Ni) and (Co,Fe) solid solutions. The microstructural analyses using SEM, TEM and 3DAPT indicate phase separation at even atomic level. This phase separation is further probed using Small-angle Scattering, providing that length scales of phase separation. Interestingly, the scattering results corroborate with the results from other microstructural investigations.

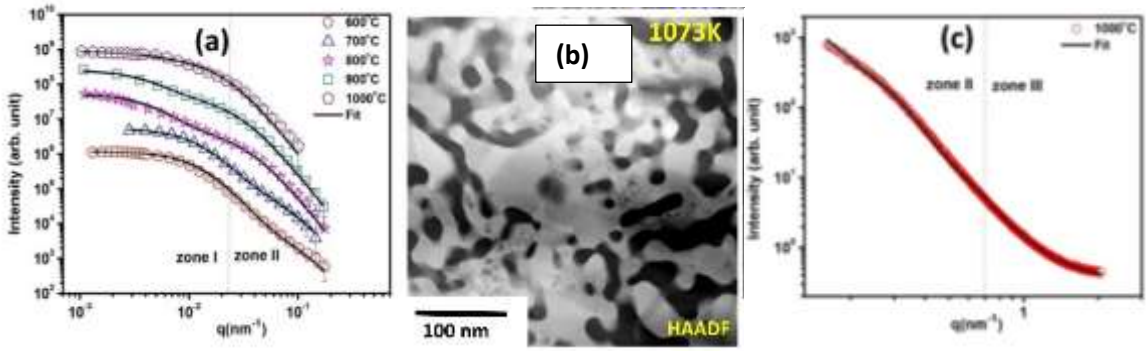

Fig. 15. (a) SANS profile of high-entropy alloy at different aging temperature. (b) Dark field TEM of sample aged at 700°C. (c) SAXS data from samples aged at 1000°C.

Since it was already revealed from TEM that the Ti-rich and Co-rich phases, present in specimen, do not possess any well-defined shape, therefore, initially, the Debye-Anderson-Brumberger (DAB) shape-independent model was employed to analyze the scattering data (Fig. 15 (a)). This model calculates scattering from randomly distributed two phase system. In this model,

the two-phase system is characterized by single length scale i.e. correlation length, which is the measure of average spacing between regions of different phases (i.e. phase 1 and phase2) present in sample. The scattering intensities in DAB model is expressed as[44, 45]:

$$I(q) = \frac{C}{(1+(q\xi)^2)^2} \qquad (23)$$

where, ξ is correlation length and C is scale factor, independent of q but depends on scattering contrast and number density.

Table 2. Extracted parameters from analysis of SANS and SAXS data using Debye-Anderson-Brumberger model

Sintering temperature(°C)				
	Zone-I (Ti-rich phase)	Zone-II (larger Co-rich phase)	Zone-II (larger Co-rich phase)	Zone-III (smaller Co-rich phase)
	ξ (nm)	ξ (nm)	ξ (nm)	ξ (nm)
600	69	8	-	-
700	70	12	-	-
800	170	29	-	-
900	181	34	-	-
1000	190	48	43	< 0.5

5. SAXS as Complementary Technique

In addition to SANS, Small-Angle X-ray Scattering is a powerful technique, where scattering contrast is governed by electron density difference between particles and matrix. As compared to the laboratory based SAXS instrument, the synchrotron-based facilities have several advantages including availability of significantly higher photon flux and wavelength tunability. Solid State Physics division, BARC developed and operates the SAXS beamline(BL-18)[46] (Fig. 16) at Indus-2 synchrotron, RRCAT, Indore (https://www.rrcat.gov.in/technology/accel/srul/beamlines/swaxs.html). It is a national facility and is also used by several users from academia and a few industries. Beamtime is allotted on the basis of accepted scientific proposals.

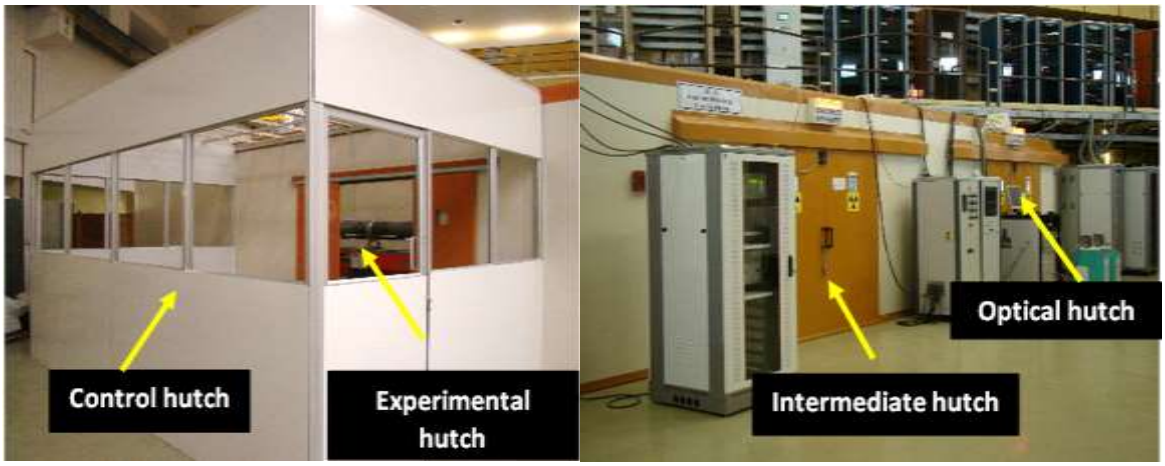

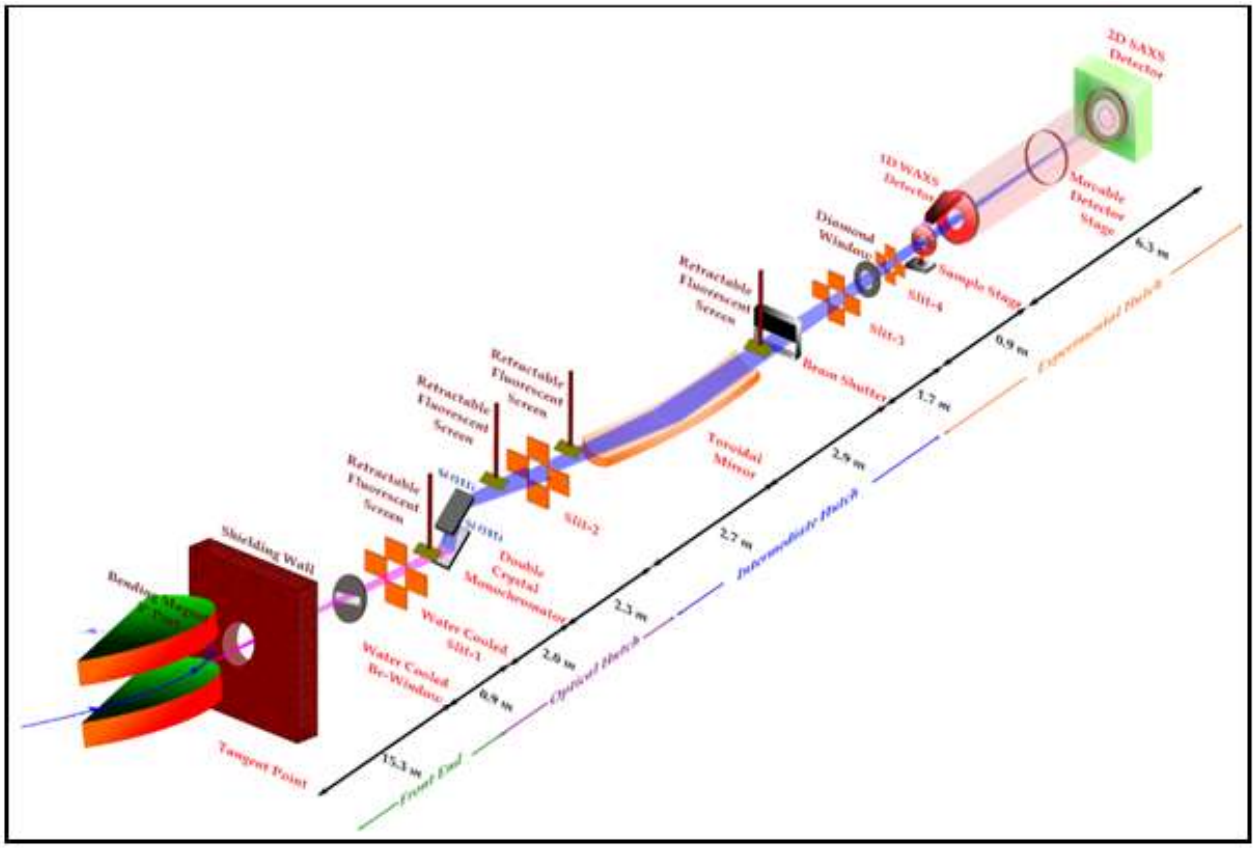

Fig. 16. SWAXS beamline (BL-18) at Indus-2 synchrotron, RRCAT, Indore.

References

1. Rehm, C.; Campo, L.; Brûlé, A.; Darmann, F.; Bartsch, F.; Berry, A., Design and performance of the variable-wavelength Bonse–Hart ultra-small-angle neutron scattering diffractometer KOOKABURRA at ANSTO. *Journal of Applied Crystallography* **2018,** *51 (1)*, 1-8.

2. Agamalian, M.; Wignall, G. D.; Triolo, R., Optimization of a Bonse-Hart Ultra-Small-Angle Neutron Scattering Facility by Elimination of the Rocking-Curve Wings. *Journal of Applied Crystallography* **1997,** *30* (3), 345-352.

3. Mazumder, S.; Aswal, V. K.; Sen, D.; Bahadur, J.; Kumar, S.; Das, A., Mesoscopic structural investigation using neutrons at Trombay: . *Neutron News* **2014,** *25*, 26-30

4. Mazumder, S.; Sen, D.; Saravanan, T.; P.R.Vijayaraghavan, A medium resolution double crystal based small-angle neutron scattering instrument at Trombay. *Current Science,* **2001,** *81*, 257.

5. Mazumder, S.; Sen, D.; Saravanan, T.; Vijatraghavan, P. R., Performance and calibration of the newly installed medium resolution double crystal based small-angle neutron scattering instrument at Trombay. *J. Neutron Res.* **2001,** *9*, 39.

6. Mazumder, S.; Sen, D.; Saravanan, T.; Vijayraghavan, P. R., A double crystal based SANS instrument at DHRUVA. *Neutron News,* **2002,** *13*, 26-30.

7. Sen, D.; Maity, A.; Bahadur, J.; Das, A.; Polshettiwar, V., Unravelling the structural hierarchy in microemulsion droplet templated dendritic fibrous nano silica. *Microporous and Mesoporous Materials* **2021,** *323*, 111234.

8. Chandra, D.; Vishal, V.; Bahadur, J.; Sen, D., A novel approach to identify accessible and inaccessible pores in gas shales using combined low-pressure sorption and SAXS/SANS analysis. *International Journal of Coal Geology* **2020,** *228*, 103556.

9. Vishal, V.; Chandra, D.; Bahadur, J.; Sen, D.; Hazra, B.; Mahanta, B.; Mani, D., Interpreting Pore Dimensions in Gas Shales Using a Combination of SEM Imaging, Small-Angle Neutron Scattering, and Low-Pressure Gas Adsorption. *Energy & Fuels* **2019,** *33* (6), 4835-4848.
10. Bal, A.; Misra, S.; Mukherjee, M.; Dutta, T. K.; Sen, D.; Patra, A.; Raja, E., Concurrent influence of geological parameters on the integrated nano-pore structure and discretized pore families of the petroliferous Cambay shale assessed through multivariate dependence measure. *Front. Earth Sci.* **2023,** *11*.
11. Bal, A.; Misra, S.; Sen, D., Nanopore Heterogeneity and Accessibility in Oil and Gas Bearing Cretaceous KG (Raghampuram) Shale, KG Basin, India: An Advanced Multi-analytical Study. *Natural Resources Research* **2024,** *33* (3), 1131-1154.
12. Kou, B.; Cao, Y.; Li, J.; Xia, C.; Li, Z.; Dong, H.; Zhang, A.; Zhang, J.; Kob, W.; Wang, Y., Granular materials flow like complex fluids. *Nature* **2017,** *551* (7680), 360-363.
13. Bahadur, J.; Das, A.; Prakash, J.; Singh, P.; Khan, A.; Sen, D., Role of trapped water on electroresponsive characteristic of silica-graphene oxide composite microspheres. *Journal of Applied Physics* **2019,** *126* (20), 204301.
14. Das, A.; Sen, D.; Bahadur, J.; Subramanian, M., Confinement induced formation of silver nanoparticles in self-assembled micro-granules. *Colloids and Surfaces A: Physicochemical and Engineering Aspects* **2019,** *577*, 185-193.
15. Sen, D.; Lakhotiya, H.; Das, A.; Bahadur, J.; Mazumder, S.; Basak, C. B., Organic–inorganic composite micro-granules by evaporation induced assembly: role of trapped water in structural evolution. *RSC Advances* **2015,** *5* (29), 22884-22891.
16. Puri, A.; Loomis, K.; Smith, B.; Lee, J.-H.; Yavlovich, A.; Heldman, E.; Blumenthal, R., Lipid-Based Nanoparticles as Pharmaceutical Drug Carriers: From Concepts to Clinic. **2009,** *26* (6), 523-580.
17. Ré, M.-I., Formulating Drug Delivery Systems by Spray Drying. *Drying Technology* **2006,** *24* (4), 433-446.
18. Gawande, M. B.; Monga, Y.; Zboril, R.; Sharma, R. K., Silica-decorated magnetic nanocomposites for catalytic applications. *Coordination Chemistry Reviews* **2015,** *288*, 118-143.
19. Luo, X.; Morrin, A.; Killard, A. J.; Smyth, M. R., Application of Nanoparticles in Electrochemical Sensors and Biosensors. *Electroanalysis* **2006,** *18* (4), 319-326.
20. Su , D. S.; Schlögl, R., Nanostructured Carbon and Carbon Nanocomposites for Electrochemical Energy Storage Applications. *ChemSusChem* **2010,** *3* (2), 136-168.
21. Yu, L.; Zhang, L.; Wu, H. B.; Zhang, G.; Lou, X. W., Controlled synthesis of hierarchical CoxMn3−xO4 array micro-/nanostructures with tunable morphology and composition as integrated electrodes for lithium-ion batteries. *Energy & Environmental Science* **2013,** *6* (9), 2664-2671.
22. Das, A.; Sen, D.; Mazumder, S.; Ghosh, A. K., Nano-structured silica coated mesoporous carbon micro-granules for potential application in water filtration. *AIP Conference Proceedings* **2017,** *1832* (1), 050094.
23. Youssef, A. M.; El-Sayed, S. M., Bionanocomposites materials for food packaging applications: Concepts and future outlook. *Carbohydrate Polymers* **2018,** *193*, 19-27.
24. Halperin, W. P., Quantum size effects in metal particles. *Reviews of Modern Physics* **1986,** *58* (3), 533-606.
25. Kar, A.; Datta, A.; Patra, A., Fabrication and optical properties of core/shell CdS/LaPO4:Eu nanorods. *Journal of Materials Chemistry* **2010,** *20* (5), 916-922.
26. Zhao, X.; Wei, C. M.; Yang, L.; Chou, M. Y., Quantum Confinement and Electronic Properties of Silicon Nanowires. *Physical Review Letters* **2004,** *92* (23), 236805.

27. Vehring, R.; Foss, W. R.; Lechuga-Ballesteros, D., Particle formation in spray drying. *Journal of Aerosol Science* **2007,** *38* (7), 728-746.
28. Wu, W. D.; Liu, W.; Gengenbach, T.; Woo, M. W.; Selomulya, C.; Chen, X. D.; Weeks, M., Towards spray drying of high solids dairy liquid: Effects of feed solid content on particle structure and functionality. *Journal of Food Engineering* **2014,** *123*, 130-135.
29. Ziaee, A.; Albadarin, A. B.; Padrela, L.; Femmer, T.; O'Reilly, E.; Walker, G., Spray drying of pharmaceuticals and biopharmaceuticals: Critical parameters and experimental process optimization approaches. *European Journal of Pharmaceutical Sciences* **2019,** *127*, 300-318.
30. Masters, K., *Spray drying handbook*. Longman Scientific & Technical ; Wiley: Burnt Mill, Harlow, Essex, England; New York, 1991.
31. Thill, A.; Spalla, O., Influence of templating latex on spray dried nanocomposite powders studied by small angle scattering. *Journal of colloid and interface science* **2005,** *291* (2), 477-488.
32. Glatter, O.; Kratky, O., *Small Angle X-ray Scattering*. Academic Press: New York, 1982.
33. L. A. Feigin; D. I. Svergun, *Structural Analysis by Small Angle X-Ray and Neutron Scattering*. Plenum Press: New York, 1987.
34. Kotlarchyk, M.; Chen, S. H., Analysis of small angle neutron scattering spectra from polydisperse interacting colloids. *The Journal of Chemical Physics* **1983,** *79* (5), 2461-2469.
35. Biswas, P.; Sen, D.; Mazumder, S.; Basak, C. B.; Doshi, P., Temperature Mediated Morphological Transition during Drying of Spray Colloidal Droplets. *Langmuir* **2016,** *32* (10), 2464-2473.
36. Biswas, P.; Sen, D.; Mazumder, S.; Ramkumar, J., Porous microcapsules comprised inter-locked nano-particles by evaporation-induced assembly: Evaluation of dye sorption. *Colloids and Surfaces A: Physicochemical and Engineering Aspects* **2017,** *520*, 279-288.
37. Kenneth, A. B., The surface evolver. *Experimental Mathematics* **1992,** *1* (2), 141-165.
38. Mondal, R.; Das, A.; Sen, D.; Satapathy, D. K.; Basavaraj, M. G., Spray drying of colloidal dispersions containing ellipsoids. *Journal of Colloid and Interface Science* **2019,** *551*, 242-250.
39. Das, A.; Mondal, R.; Sen, D.; Bahadur, J.; Satapathy, D. K.; Basavaraj, M. G., Jamming of Nano-Ellipsoids in a Microsphere: A Quantitative Analysis of Packing Fraction by Small-Angle Scattering. *Langmuir* **2022,** *38* (12), 3832-3843.
40. Sen, D.; Bahadur, J.; Das, A., Time-Resolved SAXS Investigation of Correlation-Collapse in Self-Assembled Silica Microgranules during Pozzolanic Gelling. *The Journal of Physical Chemistry C* **2022,** *126* (39), 16785-16791.
41. Datta, S. J.; Khumnoon, C.; Lee, Z. H.; Moon, W. K.; Docao, S.; Nguyen, T. H.; Hwang, I. C.; Moon, D.; Oleynikov, P.; Terasaki, O., CO2 capture from humid flue gases and humid atmosphere using a microporous coppersilicate. *Science* **2015,** *350* (6258), 302-306.
42. Mehta, S.; Bahadur, J.; Sen, D.; Singh, S.; Polshettiwar, V., Polyethylenimine assisted non-monotonic jamming of colloids during evaporation induced assembly and its implication on CO 2 sorption characteristics. *Soft Matter* **2022,** *18* (27), 5114-5125.
43. Bahadur, J.; Mehta, S.; Singh, S.; Das, A.; Maity, A.; Youngs, T.; Sen, D.; Polshettiwar, V., Interlocking dendritic fibrous nanosilica into microgranules by polyethylenimine assisted assembly: in situ neutron diffraction and CO 2 capture studies. *Materials Advances* **2022,** *3* (16), 6506-6517.
44. P. Debye, A. M. B., *J. Appl. Phys.* **1949,** *20*, 518.
45. Pedersen, J. S., *J. Appl. Crystallogr.* **1994,** *7*, 595.
46. Das, A.; Bahadur, J.; Kumar, A.; Sen, D., Performance of small- and wide-angle x-ray scattering beamline at Indus-2 synchrotron. *Rev. Sci. Instrum.* **2023,** *94*, 043902

Links to forthcoming Neutron Conferences and Workshops

January 2025

LINXS Small Angle Scattering Data Clinic IV
January 10, 2025, LINXS, Lund, Sweden
https://www.linxs.se/events/2025/01/10/linxs-small-angle-scattering-data-clinic-partner-event

February 2025

PNCMI 2025 - 15th Polarized Neutrons for Condensed-Matter Investigations
February 23-28, 2025, Dongguan, Guangdong, China
http://pncmi2025.ihep.ac.cn/

UCANS11: 11th International Meeting of the Union for Compact Accelerator-driven Neutron Sources
February 24-28, 2025, Vancouver, BC, Canada
https://www.uwindsor.ca/science/chemistry/571/ucans-11

March 2025

HERCULES 2025 - European School for Neutron and Synchrotron radiation
March 9- April 12, 2025, Grenoble, France
https://hercules-school.eu/

NMSUM 2025 - UK Neutron & Muon Science and User Meeting
March 17-19, 2025, University of Warwick, UK
https://www.isis.stfc.ac.uk/Pages/NMSUM2025.aspx

MATRAC - Neutrons and Synchrotron Radiation in Engineering Materials Science
March 23-28, 2025, Hamburg, Germany and Lund, Sweden
https://ms.hereon.de/summerschool/058651/index.php.en

July 2025

ICNS 2025 - International Conference on Neutron Scattering
July 6-10, 2025, Copenhagen, Denmark
https://www.icns2025.dk/

ICNS 2025 mini-symposium: Deuteration Matters
July 8, 2025, Copenhagen, Denmark
https://indico.ess.eu/event/3688/

ICNS 2025 mini-symposium: Magnetic SAS Data Analysis: State-of-the-Art and Future Improvements
July 9, 2025, Copenhagen, Denmark
https://indico.ess.eu/event/3704/

September 2027

SAS2027: 20th International Conference on Small Angle Scattering
September 15-19, 2025, Lund, Sweden
https://www.linxs.se/events/2027/09/12-17/20th-international-small-angle-scattering-conference-linxs-partner

Neutron Scattering Society of India

(Registered No. Maharashtra State, Mumbai, 2011 GBBSD/1696)

(For Promotion of Neutron Scattering Research in India)

C/o Solid State Physics Division,
Bhabha Atomic Research Centre, Mumbai 400085

Phones: 91-22-25595376, 25593757, 25594930

Email: neutron@barc.gov.in; URL: http://www.**nssi.org.in**

Affix your PP size recent photograph here

Application Form for Membership*

Name (in Capital letters)$: Prof/Dr/Ms/Mr (Surname last)	
Nationality:	**Date of Birth:** (dd/mm/yyyy)
Academic Qualification:	**Sex: M/F**
Profession:	**Neutron User Experience** (in yrs):
Nature of Present work:	
Affiliation: **Pin Code:**	**Residential Address:** **Pin Code:**
STD Code & Phone (O):	**STD Code & Phone (R):**
STD Code & FAX No.	**Mobile:**
Email-1:	**Email-2:**
+Details of Cheque/DD+: No.	**dated** **Bank:**
Endorsed by: (Either an existing member of NSSI or Head of the Affiliated Institute/University) **Name & Designation**	**Signature**
Date:	**Signature:**

*Life Membership fee: Rs. 1000/- (One thousand only)

Details for Online Payment:
Account Name: NEUTRON SCATTERING SOCIETY OF INDIA
Bank Name: STATE BANK OF INDIA, BARC BRANCH, MUMBAI 400085, INDIA
Account No.: 034237290776
IFSC Code: SBIN0001268

To: Secretary, ***Neutron Scattering Society of India***